

University of Cape Town
Faculty of Science
Department of Oceanography



Universiteit van Kaapstad • University of Cape Town • Universidade do Cabo da Boa Esperança

**Recovery and open-source processing of
historical ADCP records in False Bay for coastal
management purposes.**

Ethan Smith

Supervisor: Prof Marcello Vichi

Thesis presented for the degree of
Bachelor of Science Honours

October 2025

Plagiarism Declaration

I, Ethan Smith, hereby declare that the work on which this dissertation/thesis is based is my original work (except where acknowledgements indicate otherwise) and that neither the whole work nor any part of it has been, is being, or is to be submitted for another degree in this or any other university.

I empower the university to reproduce for the purpose of research either the whole or any portion of the contents in any manner whatsoever.

Declaration of use of AI

AI was used to streamline the development of the open-source processing pipeline by assisting with troubleshooting. It also used as a coding aid during the visualisation of ERA5 and WASA3 wind reanalysis data. Additionally, AI was also employed as a spell and grammar checker during the writing of this thesis.

Signature:



Date: 22 October 2025

Abstract

A clear understanding of past, present and future ocean conditions is essential for effective coastal management and planning. False Bay, a large embayment on South Africa's southwest coast, exhibits a complex hydrodynamic environment, yet observations of its physical oceanography remain sparse. This study addresses the critical lack of accessible time-series data by adapting an open-source workflow to process and recover archival Teledyne RDI Workhorse acoustic Doppler current profiler (ADCP) datasets collected between 2014 and 2017. A reusable processing and visualisation pipeline was developed and applied to ten deployments – three at Gordon's Bay and seven at Kogel Bay – producing self-describing NetCDF datasets and standardised plots for each deployment. The approach was demonstrated through a case study integrating ADCP-derived current and wave observations with ERA5 and WASA3 wind reanalysis data to illustrate potential applications in operational oceanography, including high-frequency process studies and model validation. The results highlight the value of open-source tools for extending the research utility of underused datasets and reducing reliance on costly and outdated proprietary software.

Acknowledgements

Firstly, I would like to extend my sincere gratitude to my supervisor, Prof Marcello Vichi, for his patience, support and guidance throughout this thesis. Your emphasis on quality has taught me to appreciate the time and effort required to produce meaningful scientific work. You have also helped me develop skills that I will carry forward in my career and life. Most importantly, you have shown me that discovering what doesn't work is as valuable a part of the process as finding what does.

I would also like to thank Renee Logston for granting access to the archival data used in this study. The data were provided by the Department of Oceanography at the University of Cape Town (UCT), the Council for Scientific and Industrial Research (CSIR), the South African Environmental Observation Network (SAEON), and the Institute for Maritime Technology (IMT). I acknowledge the Research Diving Unit at UCT for their role in the deployment and recovery of the ADCP instruments, and I extend my gratitude to Pieter Truter for his meticulous log keeping and assistance with deployment metadata verification. I am also grateful to Cashifa Karriem and Nadia Jabaar for their invaluable administrative support.

To A/Prof Isabelle Ansorge, thank you for inspiring and igniting in me a passion for oceanography, and for guiding me through the early stages of my career. I would also like to thank A/Prof Sarah Fawcett and A/Prof Isabelle Ansorge for selecting me as part of the science team on the SEAmester 2025 C2C cruise. The experience taught me the importance of preparation, teamwork and resilience that bled into this thesis. Thank you to Calvin Swart and Dr. Riesna Audh for your patience and support before, during, and after the cruise.

Finally, to my incredible family, partner Amber and friends, thank you for your unwavering support and encouragement throughout this year — my gratitude cannot be expressed in words. To the Honours class of 2025 — Chloë and Emily — thank you for the laughter, shared struggles, and unforgettable moments that made this year so special.

CONTENTS

1	Introduction	6
2	Literature Review	8
2.1	Surrounding Waters – Regional Influences	8
2.2	Bathymetry and Surrounding Topography	8
2.3	Wind Climate	11
2.3.1	Overview of South African Synoptic Circulation	11
2.3.2	Wind Regimes of False Bay	12
2.4	Wave Climate	15
2.5	Tides	17
2.6	Density Structure	18
2.7	Circulation.....	19
3	Methods	21
3.1	Currents	21
3.2	Winds.....	26
3.3	Waves	28
4	Results and Discussion	29
4.1	Gordon’s Bay and Kogel Bay	29
4.1.1	Velocity Timeseries.....	29
4.1.2	Rotary Spectra	31
4.1.3	Tidal Ellipses.....	33
4.2	Case Study: January 2016	35
4.2.1	Currents	35
4.2.2	Wind Reanalysis.....	36
4.2.3	ADCP Diagnostics	41
4.2.4	Waves	43
4.2.5	Conclusion	48
5	Bibliography	50
6	Appendix.....	54
6.1	ADCP Processing Environment Setup	54
6.2	Launching pycurrents in JupyterLab.....	56
6.3	Data Processing in Pycurrents:	57
6.3.1	L0 →L1: ADCP_processing_L0_L1.py	57
6.3.2	Standardized Variable Names in L1 NetCDF Files	58
6.3.3	L1 →L2: ADCP_processing_L2.py	60
6.3.4	BODC Quality Flags	61

1 INTRODUCTION

A clear understanding of past, present and future ocean conditions is essential for effective coastal management and planning. *Operational oceanography* refers to the routine provision of oceanographic information for decision-making purposes (Davidson et al., 2019). According to Davidson et al. (2019), operational oceanographic systems consist of four core components: (1) observations, (2) data management, (3) ocean prediction systems (numerical models and data assimilation), and (4) dissemination systems (Fig. 1). These components are interdependent and rely on a continuous exchange of information.

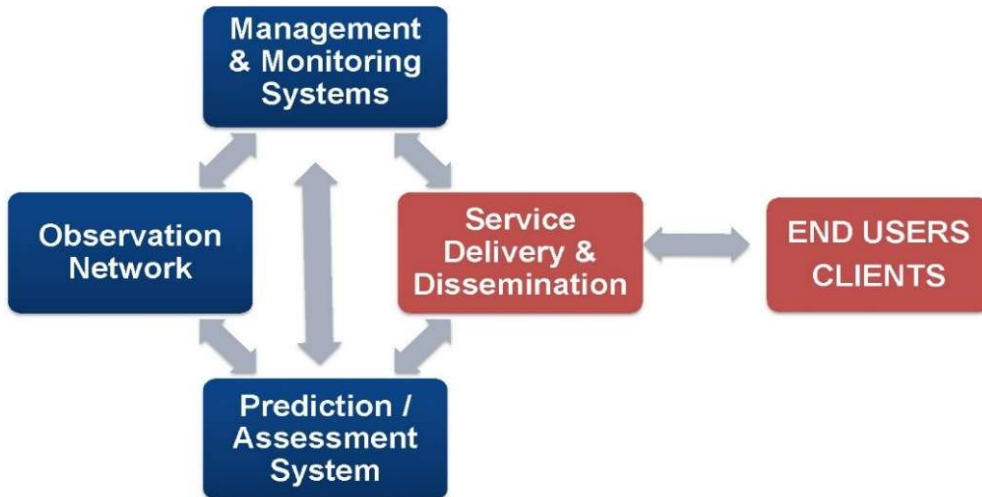


Figure 1)The four core components of operational oceanographic systems, their interrelationships and their connections to end users (from Davidson et al., 2019)

The synergy between prediction and observation systems determines the quality of products available to stakeholders and underscores the importance of sustained ocean observations (Davidson et al., 2019). Operational oceanography can be viewed as a *value chain* – transforming ocean observations into products that meet societal needs (Robinson and Lermusiaux, 2001). Observations, whether *in situ* or remotely sensed, form the first link of this chain and are closely tied to data management. The quality of data management dictates the usability of the observations, making these two components critical to the success of any operational oceanographic system.

Observational data are combined with numerical models through data assimilation to estimate ocean conditions. These models can be used to hindcast and forecast ocean states at various spatio-temporal scales. However, their predictions must be evaluated against observations to assess model performance and identify areas for improvement.

Establishing an operational oceanographic system is a time-, skill-, and resource-intensive challenge – one that is currently predominantly led by institutions in the Global North. South Africa has recently made progress toward addressing this gap through the Sustainable Modelling Initiative: a South African Approach (SOMISANA). *Somisana* means ‘to work together’ and its mission is to develop “an ocean modelling hub and platform that promotes the inclusive development of local expertise and that produces and provides state-of-the-art ocean information, tools and research that is visible and accessible to all”. This initiative is a step towards a locally lead operational oceanographic system.

For developing countries, such as South Africa, the financial and technical barriers to establishing and maintaining operational systems remain significant. Under these circumstances, it becomes essential to maximise the utility of existing resources — first by improving access to available data; and second, by processing these data into forms suitable for use with ocean prediction systems.

Over the past three decades, traditional sector-by-sector approaches to natural resource management have moved toward system-oriented, multi-stakeholder frameworks. Within the coastal marine sphere, operational oceanographic systems form a crucial part of this integrated management approach. Such an approach is important where many stakeholders depend on limited marine resources, and where sustainability is directly tied to livelihoods.

False Bay exemplifies these challenges (Fig. 2). It is a large, square-shaped embayment ($\sim 1130 \text{ km}^2$) on the southwest coast of South Africa's Western Province (Flemming, 2024). The bay's oceanography is highly dynamic across spatial and temporal scales with conditions ranging from cold, seasonally pulsed upwelling to periodic warm water intrusions (Largier *et al.*, 1992; Dufois and Rouault, 2012). These conditions support high biological diversity (Pfaff *et al.*, 2019).

The bay's southward-facing mouth exposes it to high-energy wave systems originating from the South Atlantic sector of the Southern Ocean. The wave climate of False Bay has been the subject of several studies, which have identified the occurrence of significant wave events that contribute to environmental risks such as shoreline erosion and infrastructure damage (Fourie *et al.*, 2015; Coleman, 2019; Veitch *et al.*, 2019; de Vos, 2022). In some areas, the shoreline has receded up to 30 m within 11 years, damaging coastal infrastructure and transport routes (Fourie *et al.*, 2015). These risks are expected to intensify under climate change. A projected southward shift of mid-latitude cyclones is likely to increase the incidence of direct southerly wave events, enhancing coastal erosion and flooding hazards along the bay's shores (Climate Systems Analysis Group, 2016; Veitch *et al.*, 2019).

Economically, False Bay is a major centre for coastal tourism, with direct expenditure exceeding R900 million per year, 80 % of which is concentrated along the western shore (Turpie *et al.*, 2017; Pfaff *et al.*, 2019). The northern and eastern sections are frequently exposed to a high-energy wave climate, posing risks to infrastructure and safety for users such as rock anglers, surfers, swimmers, kayakers, and divers.

A synthesis of False Bay research by Pfaff *et al.* (2019) highlighted a critical lack of reliable oceanographic time-series data, compromising the ability to detect long-term trends in the bay's physical environment. Routine, publicly available measurements — essential to an operational oceanographic system — are constrained to accessible nearshore sites. *In situ* time-series are typically limited to one or a few locations (as in this study), meaning that assessments of spatial variability remain largely speculative.

The recommended priorities that align with operational oceanography can be summarised as follows:

- **Repeat linked observations:** Conduct long-term, multi-scale measurements of physical, chemical and biological parameters in a synchronised manner to capture system interactions and feedback.
- **Technology integration:** Use automated systems for efficient and broad spatio-temporal monitoring while improving data processing, management and accessibility.
- **Advanced data systems:** Develop robust data management frameworks and analytical tools to handle large multidisciplinary datasets.
- **System-level analysis and modelling:** Promote studies using numerical models to examine system components and interactions.

Despite the availability of *in situ* observations, many datasets remain underutilised due to limited accessibility and inadequate data management practises. High-resolution wave and current data from

acoustic Doppler current profilers (ADCPs) provide valuable insights into coastal hydrodynamics, yet their utility is often constrained by costly proprietary processing software. This study addresses these limitations by collating, organising, and reprocessing archival ADCP data to extend its research utility

In this thesis we present a literature review of the physical oceanography of False Bay and adapt an open-source processing solution for Teledyne RDI Workhorse ADCP data collected between 2014 and 2017 by the Department of Oceanography at the University of Cape Town. A reusable processing and visualisation pipeline was developed and applied to ten repeat-deployments – three at Gordon’s Bay and seven at Kogel Bay – producing self-describing NetCDF datasets containing georeferenced velocities profiles and standardised plots for each deployment. Wind reanalysis data and wave observations derived from the ADCP were incorporated to illustrate potential research applications, with an emphasis on high-frequency variability and model validation to support future coastal management in False Bay.

The methods chapter outlines the process of working with archival data, including metadata validation and the selection and adaptation of a suitable open-source software framework. It also details the user-specified processing options and data handling steps. The results demonstrate the functionality of the pipeline through visualisations from two overlapping deployments (December 2015 to March 2016) near Gordon’s Bay and Kogel Bay. A case study of in situ current and wave data, combined with wind reanalysis, illustrates the operational oceanographic applications of the processed data and the developed pipeline.

2 LITERATURE REVIEW

2.1 SURROUNDING WATERS – REGIONAL INFLUENCES

Conditions in False Bay vary from wind-driven upwelling typical of the southwest coast to warm water intrusions from the Agulhas Current off the Agulhas Bank to the southeast (Isaac, 1937; Largier *et al.*, 1992; Pfaff *et al.*, 2019). Cape Point, and by extension False Bay, forms the western extremity of the Western Agulhas Bank (WAB) (Isaac, 1937; Largier *et al.*, 1992).

An overview of the dynamics of the WAB is essential for understanding circulation in False Bay. The WAB is a transitional shelf region which has been divided into three subregions by Largier *et al.* (1992). These are the coastal region, the mid-shelf region, and the shelf-edge region. The Western Agulhas Shelf Processes experiments (WASP) used mooring arrays to determine the processes affecting the different regions (Largier *et al.*, 1992). It was established that the three subregions act somewhat independently where the shelf is wide. The shelf narrows dramatically toward Cape Point which results in the comingling of currents and interactions between density structures (Bang and Andrews, 1974; Largier *et al.*, 1992).

One key outcome of these interactions is the development of prominent frontal features near the bay’s entrance. The coastal and shelf-edge frontal systems merge to the south of False Bay’s entrance and are observed as an intense front and jet named the Good Hope Jet (Bang and Andrews, 1974). The Bay is exposed to processes on the WAB and in the open ocean. These processes interact with local wind forcing to drive circulation within the Bay (Wainman, Polito and Nelson, 1987).

2.2 BATHYMETRY AND SURROUNDING TOPOGRAPHY

False Bay is a square-shaped embayment on the southwest coast of South Africa’s Western Province. The central coordinates of the bay, as presented by Flemming (2024), are $34^{\circ}14.0'S$ and $18^{\circ}39.0'E$ (Blue cross in Fig. 2). The maximum meridional extent of the bay is ~35 km, measured from the northern shore to latitude $34^{\circ}23'S$, which intersects Cape Hangklip south-east of the bay’s centre (Flemming, 2024). The

maximum zonal extent is a ~39 km stretch between Fish Hoek and Gordon's Bay (Flemming, 2024). The embayed area is approximately 1130 km^2 (Flemming, 2024).

The average depth is ~41 m and the deepest point near the entrance is ~90 m (Taljaard, van Ballegooyen and Morant, 2000). The bay is open to the sea at its southern extent, which is defined by Cape Point and Cape Hangklip to the west and east respectively. The northern extent is characterized by long sweeping beaches, which are separated halfway by eroding cliffs between Kapteinsklip and Swartklip. The boulders and cliffs of the rocky eastern and western shores are interspersed with small sandy beaches.

The bay has been split into four geographical zones which categorize sectors of the bay with similar bathymetric features (Atkins, 1970a). A description of the zones follows:

Northern Zone

The northern zone is categorized by a gentle slope (~1:400) with a fragmented rocky bottom to the west and a predominantly sandy bottom to the east (Mallory, 1970).

Western Zone

The bathymetry of both the eastern and western peripheries is steep (Fig. 2). The western zone is characterized by several large rocky features, listed here from north to south: Roman Rock, Seal Island & York Shoal, East Shoal, Whittle Rock and Rocky Bank (Mallory, 1970). These features consist primarily of granite and sandstone, and form part of the Cape Granite and Table Mountain Group of geological formations (Flemming, 2024).

Eastern Zone

North-South running ridges, some of which are ~17 km long and ~300 m wide characterize this region (Mallory, 1970). They are comprised of shale and form part of the Malmesbury Group (Flemming, 2024).

Central Zone

Two distinct terraces, one between 30 and 45 m, the other between 50 and 55 m, exist in the bay and are indicative of Pleistocene (2.6 Ma to 11 700 ka) sea-level stillstands (Flemming, 2024).

Given this pre-historic context, the bay itself can be seen as the southernmost extension of the Cape Flats, a sandy valley which links the Cape Peninsula on the west to the mainland on the east. The eastern side of the bay is rimmed by the Hottentots Holland Mountains which range between 1100 and 1400 m (Bonnardot, Planchon and Cautenet, 2005). The Cape Peninsula mountain to the west has a slightly lower range of between 600 and 1100 m (Jury, 1991). The intricate orography of the terrain is known to modify the wind field over the Bay (Jury, 1991), and is shown in Fig 3.

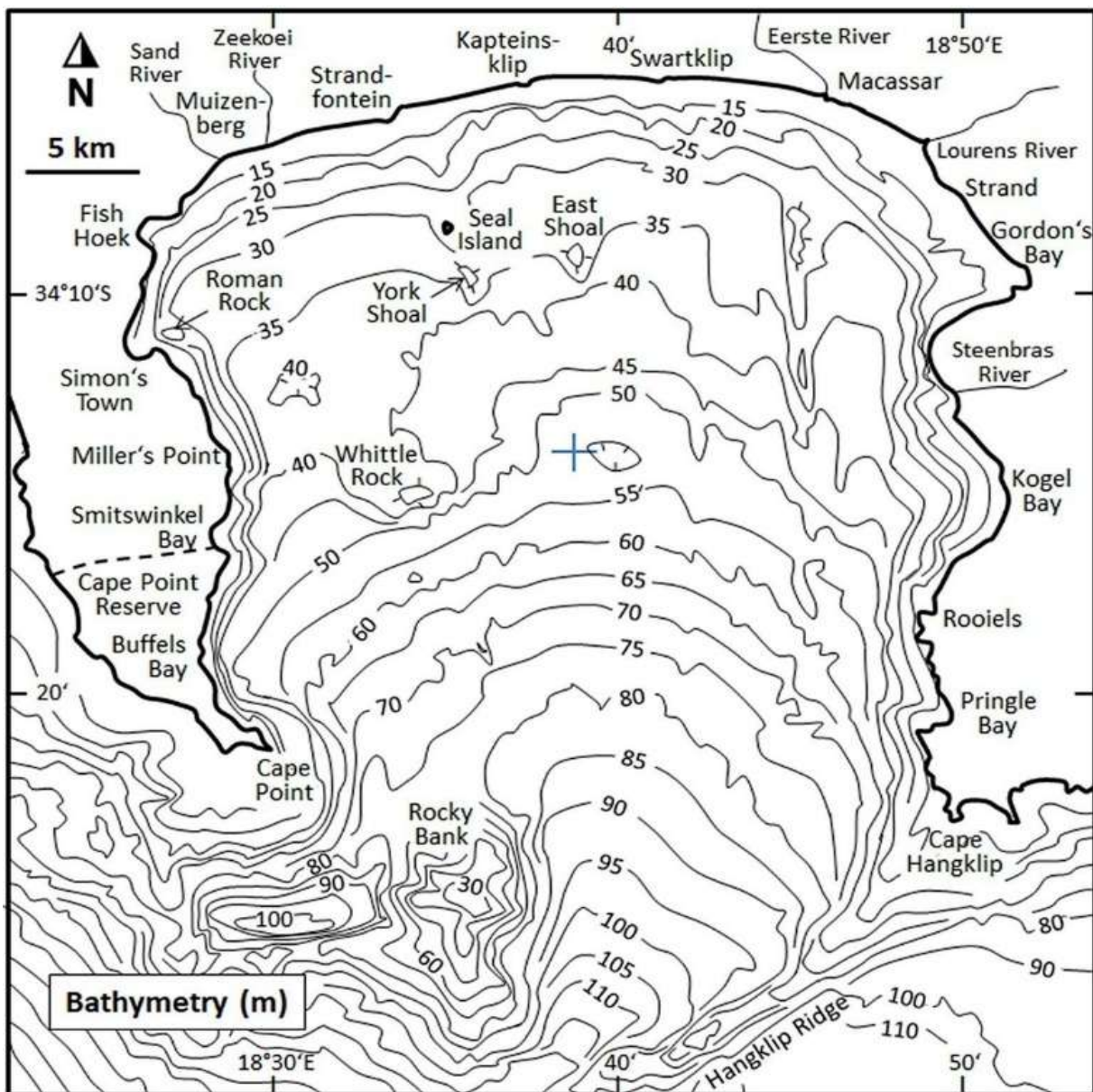


Figure 2) The bathymetry of False Bay and the names of well-known locations and features. The blue cross indicates the centre of the bay (From Flemming, 2024; based on Glass, 1976)

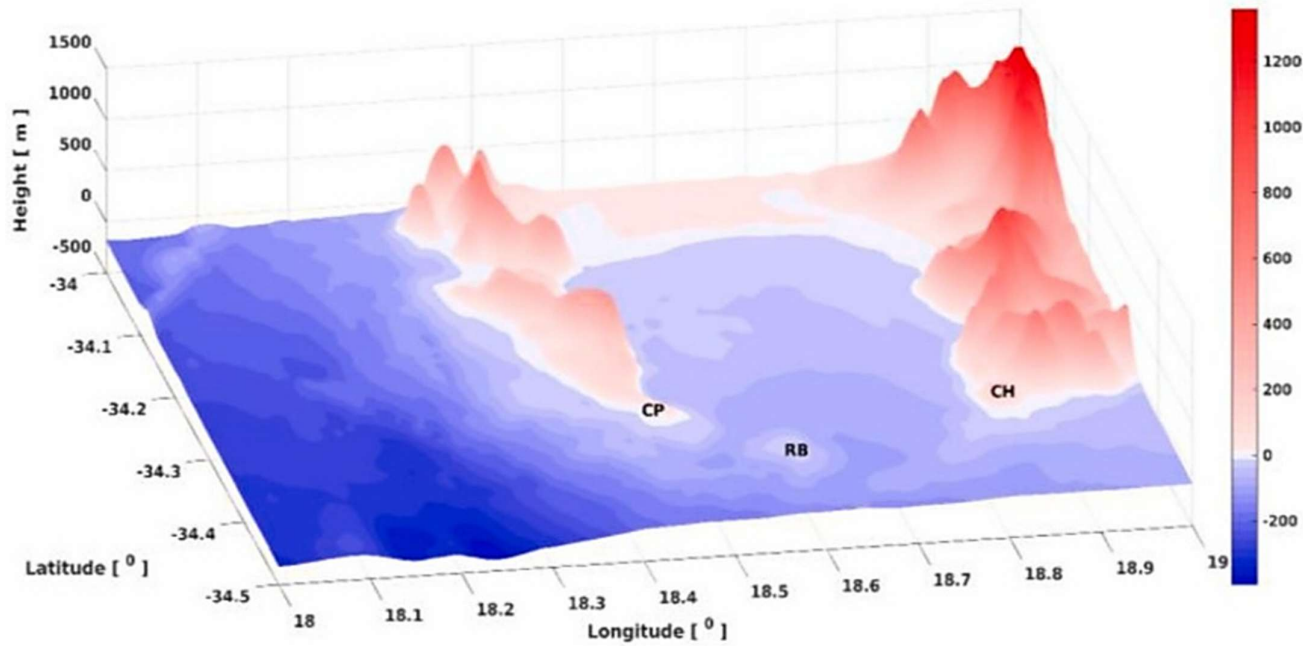


Figure 3) Bathymetry of, and orography surrounding False Bay. Cape Point (CP), Rocky Bank (RB) and Cape Hangklip (CH) are shown (From Daniels et al., 2022).

2.3 WIND CLIMATE

2.3.1 Overview of South African Synoptic Circulation

South African weather is primarily seasonal and dominated by large scale synoptic circulations. These result from interactions between the South Atlantic high pressure cell (SAH) and mid-latitude pressure systems which are both associated with the upper-level westerlies. Synoptic systems that affect the coast are controlled by the eastward propagation of atmospheric Rossby waves (Wainman, Polito and Nelson, 1987; Gründlingh, Hunter and Potgieter, 1989; MacHutchon, 2006). Wind over False Bay is influenced by the nature and time scale of synoptic weather systems and local orographic effects (Jury, Kamstra and Taunton-Clark, 1985; Gründlingh, Hunter and Potgieter, 1989)

Among the main synoptic systems, **coastally trapped lows and cold fronts** contribute significantly to local wind variability over False Bay. Several synoptic types are used to explain the general atmospheric circulation along the coast. The SAH guides atmospheric fronts north-westward toward the South African coast (Gründlingh, Hunter and Potgieter, 1989). This occurs over the South-Atlantic sector of the Southern Ocean. Approaching cold fronts (Mid-latitude cyclones) typically generate coastally trapped low pressure systems on the west coast (Gill, 1977). These propagate anti-clockwise along the coast and influence local winds as they move along. The passage of a coastally trapped lows are preceded by warm, often strong, offshore Foehn (Berg) winds and followed by cool onshore winds (Gill, 1977).

Coastally trapped lows are linked to the subsequent passage of cold fronts, which further modify local wind fields. Cold fronts follow coastally trapped lows, bringing north-westerly winds ahead of the front and a rapid incursion of cold, high latitude air masses after their passage (Jury, Kamstra and Taunton-Clark, 1985; Gründlingh, Hunter and Potgieter, 1989). Fronts are typically succeeded by southerly meridional flow due to a strong pressure gradient west of the cyclone. This flow generally lasts a day, after which the ridging of the SAH induces strong south-easterly winds, particularly during austral summer (DJF). These dynamics typically cycle on a weekly basis (5-7 days) and are seasonal in nature (Gründlingh, Hunter and Potgieter, 1989).

The strength and frequency of these systems vary seasonally, reflecting shifts in larger-scale circulation patterns. Cold fronts and coastal lows are generally weaker in summer due to the southward displacement of the Inter Tropical Convergence Zone, while the opposite occurs in winter. Summer cycles are marked by 3-5 days of southeasterlies, with local orographic effects producing winds speeds exceeding 30 knots at Cape Point (Le Roux, 1975).

In addition to these seasonal variations, the vertical stratification of the atmosphere influences winds over False Bay. The height of the inversion layer (an unstable atmospheric layer where temperature increases with height) is modulated by the passage of these weather systems and affects the behaviour of the winds over the bay (Jury, 1991; Bonnardot, Planchon and Cautenet, 2005; Daniels *et al.*, 2022). The vertical extent of surface winds reaches a minimum during coastally trapped lows, and can create a wind shadow in the lee of the eastern mountains surrounding False Bay (Jury, Kamstra and Taunton-Clark, 1985; Wainman, Polito and Nelson, 1987). This is the cause of a pronounced slowdown in winds in the north-east of the bay during June, July and August (Atkins, 1970b).

Beyond these frontal and inversion-related processes, the other relevant synoptic scale disturbances are **cut-off lows**, which exert a significant influence along the South African coast. Cut-off lows (COLs) are a class of low pressure system that cross the South African coast ~11 times a year (Singleton and Reason, 2007). These systems become detached from the main jet stream and therefore move independently, sometimes becoming stationary (Singleton and Reason, 2007). Extreme wave conditions, with significant wave heights and peak periods exceeding 10 m and 20 s, respectively, are associated with COLs (Boyd *et al.*, 2014).

2.3.2 Wind Regimes of False Bay

The observed wind field in False Bay is highly variable and complicated. Wainman *et al.* (1987) analysed time series data from anemometers and found that correlations between stations was poor (< 0.6). The spatially varying wind field over False Bay was described as a synoptic sequence by Jury (1984). This classification divides the wind field into several distinct regimes, each shaped by interactions between the synoptic scale forcing and local orographic effects.

South-west regime: South-westerly winds are associated with the ridging SAH following the passage of a cold front. Due to local orographic effects near Walker Bay, south-east of False Bay, the wind field becomes uniformly southerly and strengthens as the pressure gradients increase (Jury, 1984; Largier *et al.*, 1992). This is illustrated in Fig 4a.

South-east regimes

In contrast, south-easterly winds dominate under different conditions, which are further divided into deep and shallow regimes.

Deep south-east regime: During southerly meridional flow deep southeasterlies flow over the surrounding mountain ranges and are associated with accelerated wind speeds across the bay, as well as the development of a strong easterly downslope jet in the lee of the Kogelberg mountains. The deep regime can transition into the shallow regime when a low-level subsidence inversion caps the south-easterly winds below the surrounding mountains. This signals the development of the shallow south-east regime. This is illustrated in Fig 4b.

Shallow south-east regime: The ridging process of the SAH lowers the height of the inversion layer and blocks the surface wind from flowing over the Hottentots Holland mountain range. The mountain range and inversion constrain the wind to ~600 m vertical extent and deflect it seaward (Wainman, Polito and Nelson, 1987). The resulting surface winds accelerate past Cape Hangklip and a wind shadow can develop in the lee of the Helderberg Mountains (Wainman, Polito and Nelson, 1987). This is known to influence the

circulation near Gordon's Bay. The data analysed by Wainman et al. (1987) indicate that these winds entering the bay are deflected (by local orographic effects) to become increasingly southerly. The shift from a deep to shallow south-east regime usually occurs over three days (Jury, 1984; Jury, Kamstra and Taunton-Clark, 1985), and is illustrated in Fig 4c.

North-west regime: North-westerly winds signal the approach of a cold front after the passage of a coastally trapped low and become far more common during winter. Flow over the Table Mountain range deflects the wind such that it becomes uniformly northerly over False Bay. The winds at the mouth of the bay are typically stronger and more north-westerly to westerly due to topographic steering at Cape Point. This is illustrated in Fig 4d.

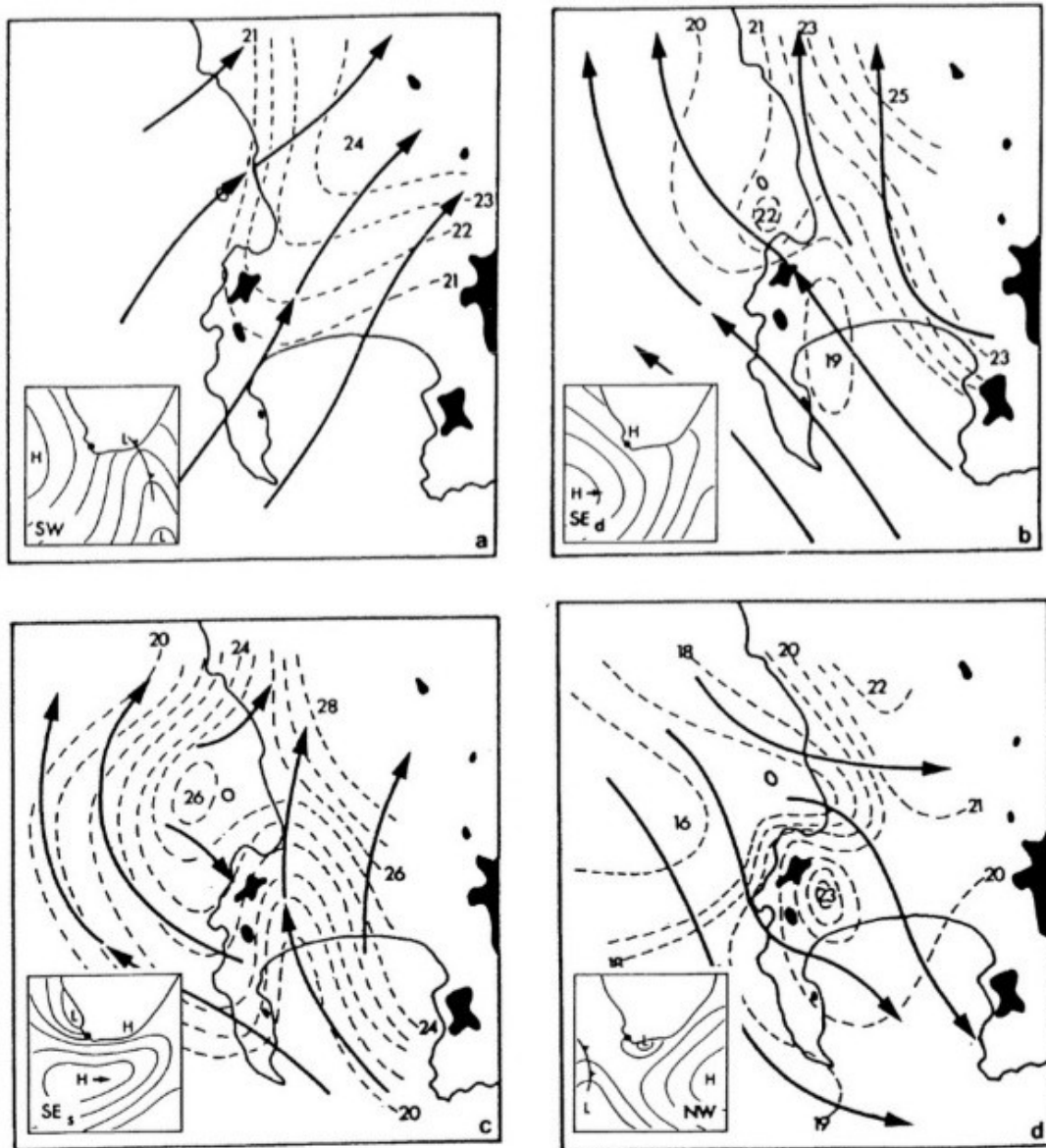


Figure 4) Four wind phases and associated synoptic systems. Southerly meridional flow - a; Ridging SAH - b & c, Coastal low – d. Isobars show truncated values of mean sea level pressure in hPa (Jury, 1984)

These wind regimes are captured in high-resolution model outputs from the South African Weather Service (SAWS). Fig. 5 shows the 10 m flow streamlines associated with each wind regime and is based on outputs from the SAWS operational Unified Model which has a 4.4 km horizontal grid resolution (Cullen, 1993; Brown *et al.*, 2012). The model output indicates that higher winds speeds are expected over the bay during south-west and deep south-east regimes, compared to slower speeds during the other two regimes. Early observational studies by Le Roux (1975) and Gründlingh *et al.* (1989) measured average wind speeds of $\sim 5\text{--}7 \text{ m} \cdot \text{s}^{-1}$. These historical measurements correspond well to recent observations (Bonnardot, Planchon and Cautenet, 2005; Daniels *et al.*, 2022) and numerical simulations (Coleman, 2019; Salonen, 2019; de Vos, 2022).

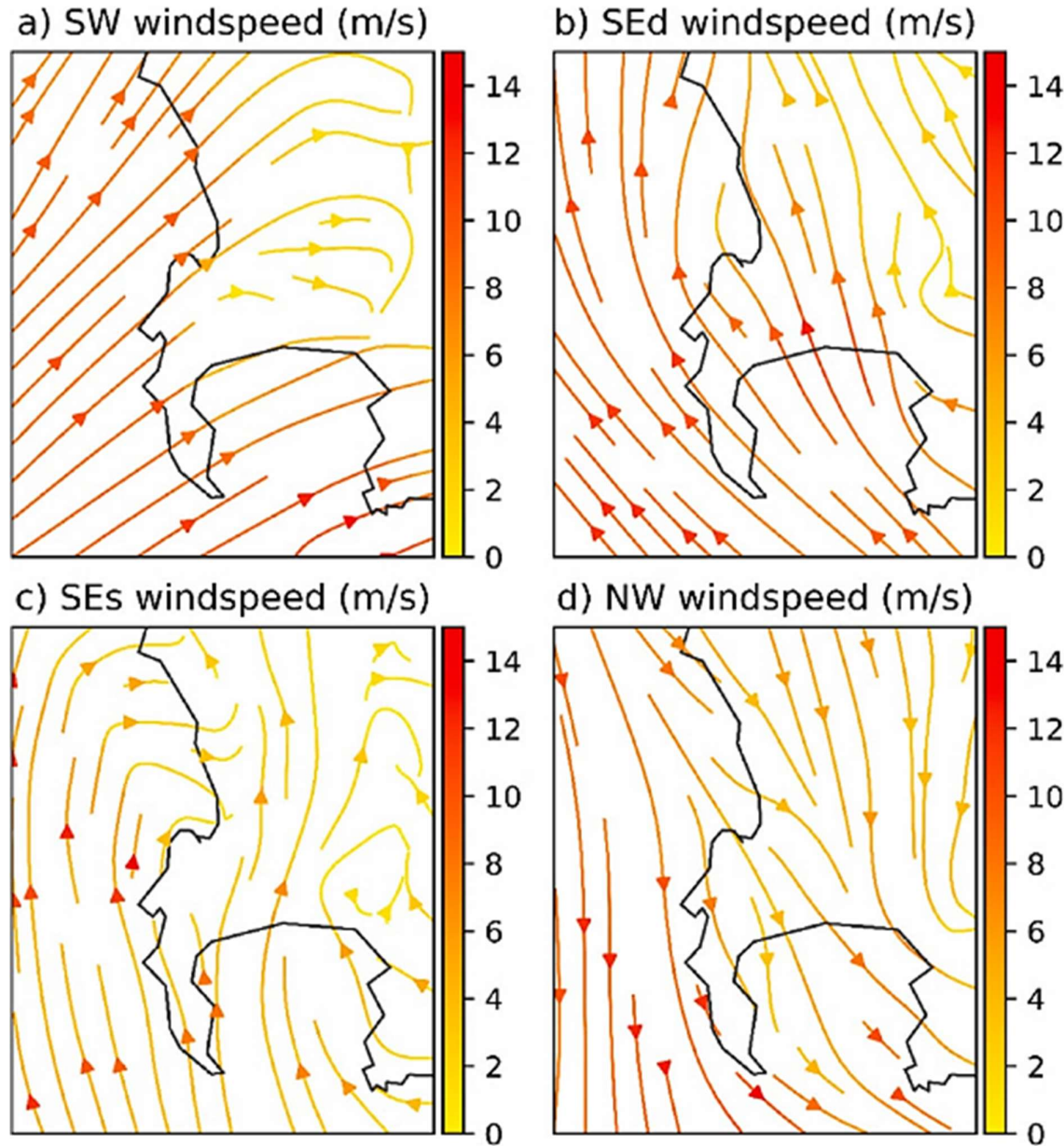


Figure 5) Wind streamlines in $\text{m} \cdot \text{s}^{-1}$, for the four primary wind regimes that affect False Bay (From Daniels *et al.*, 2022; after Jury, 1987)

2.4 WAVE CLIMATE

Surface ocean waves result from an exchange of energy and momentum between the atmosphere and ocean. Their growth depends on wind speed, fetch, and duration (Salonen, 2019; Ramos *et al.*, 2021). The dominant wave systems which impact the coastline near False Bay are generated by eastward-propagating cold fronts originating in the South Atlantic sector of the Southern Ocean (Shillington and Wyndham Harris, 1978; Salonen, 2019). As a result, the predominant swell impacting False Bay arrives from the southwest (Shipley, 1964; Shillington and Wyndham Harris, 1978).

The swell arriving in False Bay is modified by **dispersion processes**. Generation zones of swell waves are characterized by a broad wave spectrum. This means that the wave energy is spread over a wide range of frequencies and directions. As waves propagate away from their generation zone, frequency and directional dispersion processes cause the wave spectrum to narrow, and so organised swell is formed (Veitch *et al.*, 2019).

The **seasonal cycle of swell** affecting False Bay is dependent on the spatio-temporal variability of cold fronts, which is linked to the seasonal variability of the upper-level westerlies (Taljaard *et al.*, 1969; Veitch *et al.*, 2019). In austral summer (DJF), typical wave heights are between 2 and 3 m, although anomalous northward occurrence of cold fronts can generate larger seas (Joubert, 2008; Massel, 2017). Peak periods of between 8 -16 seconds are expected with the passage of cold fronts south of Cape Point (van Verwolde, 2004). Greater wave heights of between 4 and 5 m are observed in winter months (JJA) (Massel, 2017).

Long-term observations confirm this seasonal cycle. The Cape Point wave record, maintained by the Council for Scientific and Industrial Research (CSIR) and Transnet, consists of buoy measurements at Slangkop (1980-1993) and Cape Point (1994-2010). Analysis of significant wave heights (H_s) and peak periods (T_p) by Veitch *et al.* (2018,2019) revealed a pronounced seasonal signal, with the largest, longest-period, and most energetic waves occurring in austral winter. These waves carry a strong westerly component which is consistent with increased frontal activity during winter months (Veitch *et al.*, 2019).

Veitch *et al.* (2019) remarked that the seasonal cycle of waves is ‘consistent with’ the seasonal variation in the number and depth of cold fronts in the South Atlantic and Atlantic sector of the Southern Ocean. During austral winter, the wave generation zone moves closer to South Africa due to the northward shift of the upper-level westerlies. This brings the primary wave generation closer to the coast of South Africa, resulting in the greater observed H_s values (Taljaard *et al.*, 1969). Fig. 6 shows the wave directions throughout the year, with a clear dominance of south-easterly waves (Veitch *et al.*, 2019).

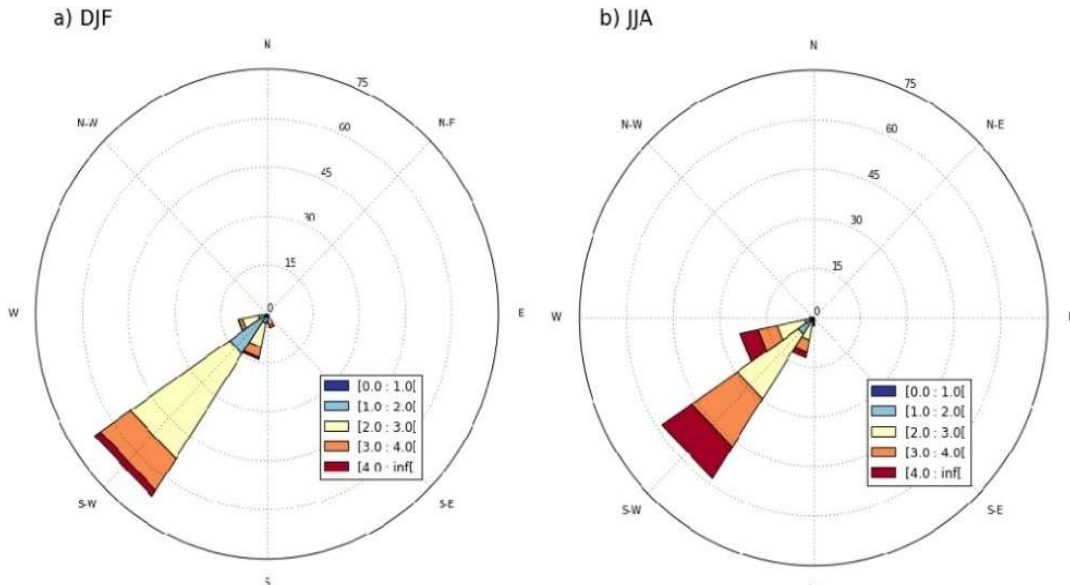


Figure 6) Wave rose showing the observed mean wave direction (θ) and significant wave height (H_m0) from the Cape Point wave record for the period from 2000 to 2010 (From Veitch *et al.*, 2019).

This relationship is upheld by a National Centers for Environmental Prediction (NCEP) reanalysis-based analysis by Salonen (2019). They generated seasonal wave roses which show that the mean wave direction affecting the bay lies between 210° and 240° true, with peak periods between 11.5 and 13.3 seconds (Fig. 7). The observed wave parameters and those derived from the reanalysis product are in general agreement, reinforcing the role of large-scale atmospheric forcing on the swell entering the bay.

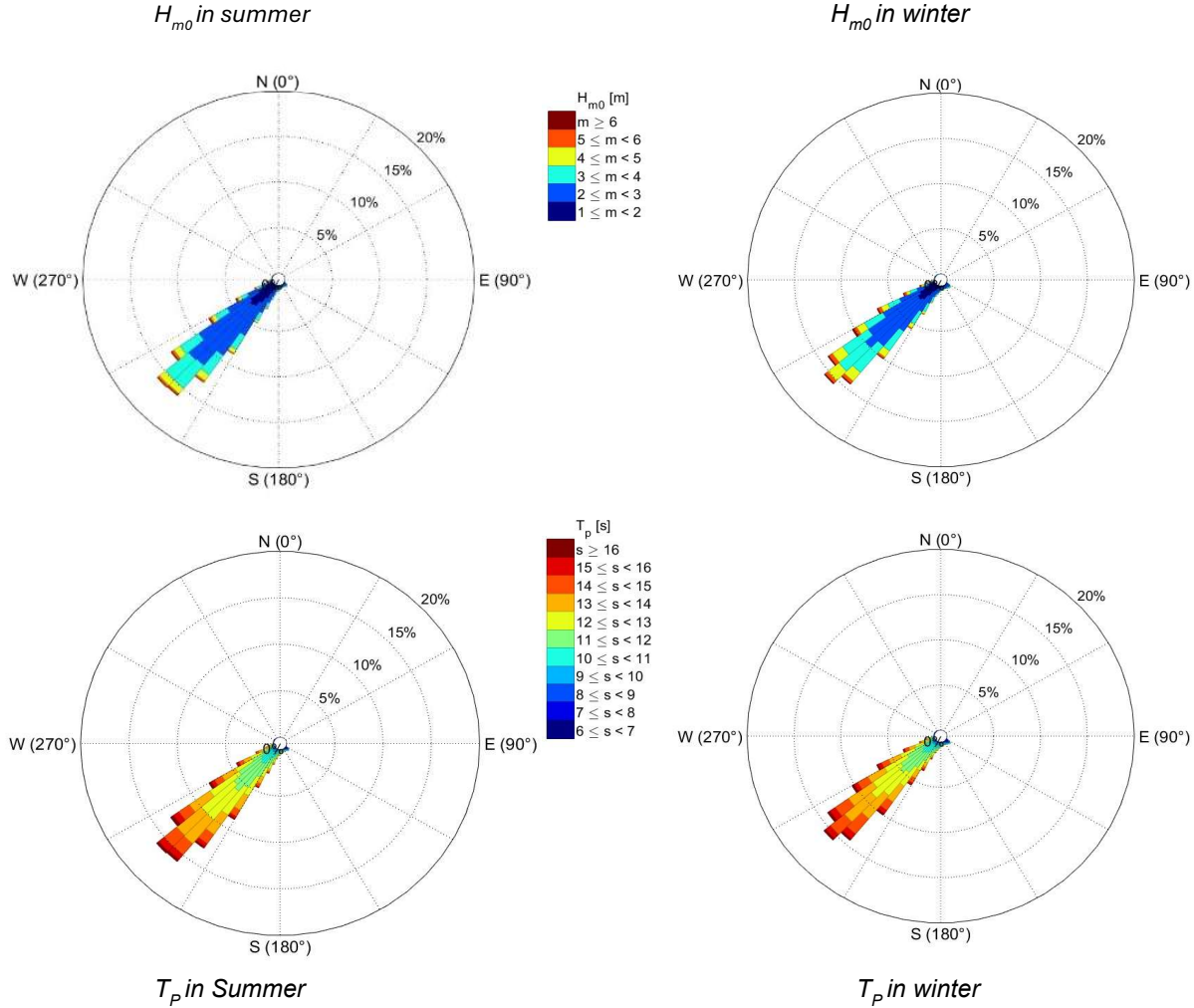


Figure 7) Seasonal wave roses showing the mean wave directions from the NCEP reanalysis dataset (Kalnay et al., 1996) for a point outside of False Bay ($34.5^\circ S, 18.5^\circ E$). Significant wave heights are shown by roses a and b, whereas peak periods are shown by roses c and d. Each rose shows the proportions associated with 5° bins (From Salonen, 2019).

While these large-scale processes set the overall wave climate, local **bathymetric features** strongly modulate the propagation of swell within False Bay. The Cape Peninsula shelters the western side of the bay from the predominant south-west swell (Shipley, 1964; Boyd et al., 2014; Salonen, 2019). This blocking of wave energy leads to a nearly 2 m difference between wave heights observed inside and outside of the bay (Boyd et al., 2014). The eastern periphery generally experiences greater wave heights compared to the west (Boyd et al., 2014).

Rocky Bank (Fig. 8) further modifies incoming swell through refraction and spatial focussing (Shipley, 1964). Salonen (2019) investigated this with a series of numerical experiments using the Simulating Waves Nearshore (SWAN) model. They observed convergent wave energy within the bay resulting from refraction and spatial focussing of swell by Rocky Bank, as well as a clear reduction of coastal wave heights in the lee of this feature. The magnitude of the reduction is proportional to the peak period of the predominant incoming swell. According to Salonen (2019), these processes render the eastern periphery of the bay, known to local anglers as the “Death Coast”, especially vulnerable to hazardous wave conditions.

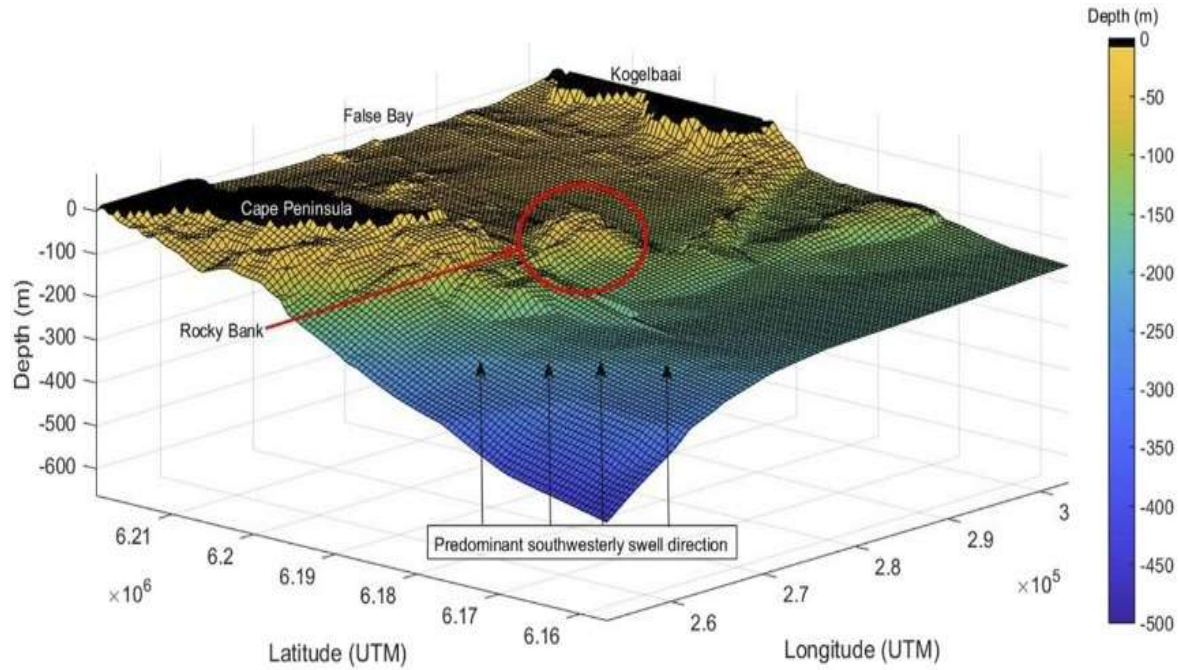


Figure 8) Three-dimensional visualisation of Rocky Bank. The viewing angle is consistent with the predominant swell direction (From Salonen and Rautenbach, 2021)

While geographical features within and surrounding the bay play a critical role in shaping the spatial distribution of the incoming swell, additional modification of the wave field arises from **local atmospheric forcing**. Orographic modification of winds affecting the bay give rise to a complicated, spatially variable wind field. The importance of wind-driven waves within embayments is made clear throughout the literature (Jury, 1991; Coleman, 2019; Salonen, 2019; Daniels *et al.*, 2022; de Vos, 2022). In False Bay, Daniels *et al* (2022) set up experiments using the SWAN model forced by wind products of various resolutions to isolate orographic effects. They confirmed that waves on the western periphery are primarily generated by local winds, rather than incoming swell. In contrast, the eastern periphery is more exposed to the predominant swell. These findings were attributed to the high-resolution wind fields provided by the Wind Atlas of South Africa (WASA) reanalysis product.

2.5 TIDES

Tides in False Bay are modest in range and play a role in driving currents and modulating shoreline processes. The tidal range in False Bay is approximately 0.8 m and 1.6 m during neap and spring cycles respectively (Gründlingh, Hunter and Potgieter, 1989). Ebb and flood tides generate noticeable currents under calm wind and wave conditions, particularly along the shoreline and in the shallow north of the bay (Atkins, 1970b; Wainman, Polito and Nelson, 1987). High tides and intense storms are the main contributors to coastal erosion in False Bay, and have resulted in damage to coastal infrastructure such as railways and beach resorts (Fourie *et al.*, 2015). Preliminary observations by Atkins (1970b) showed that ebb and flood tides act to modulate wind-driven currents within the bay.

Gründlingh et al. (1989) investigated this further by deploying an array of current meters in the lower half of the water column near the mouth of the bay during the summer of 1986/87 (DJF). The semi-diurnal tidal constituent (K2) was identified as the most significant, especially in the meridional component (N-S), and increased in magnitude from west to east (Gründlingh, Hunter and Potgieter, 1989). Semi-diurnal tidal currents were aligned along a north-northeast to south-southwest direction (in and out of the bay) with flow rates of $2.6 - 3.8 \text{ cm} \cdot \text{s}^{-1}$ (Gründlingh, Hunter and Potgieter, 1989). The diurnal tidal component (K1) had a flow rate of comparable magnitude (Gründlingh et al., 1989) ($2.2 - 3.3 \text{ cm} \cdot \text{s}^{-1}$), but was more evident in the zonal (E-W) current (Gründlingh, Hunter and Potgieter, 1989).

Modelling studies have further clarified how tidal currents interact with the bay's bathymetry as well as their vertical structure. A modelling study by Coleman (2019) supported the observation of a decoupling of surface and bottom flows and described bottom flows as weak tidal currents with a magnitude $\leq 10 \text{ cm} \cdot \text{s}^{-1}$. Neap and spring tidal currents were similar under flood and ebb conditions (Coleman, 2019). Flood tidal currents had a typical range of $2 - 10 \text{ cm} \cdot \text{s}^{-1}$ throughout the bay. They accelerated around Cape Point, over Rocky Bank and along the steep eastern shoreline (Coleman, 2019). Ebb tidal currents had a comparable magnitude range of $2 - 6 \text{ cm} \cdot \text{s}^{-1}$. Magnitudes reached $10 - 25 \text{ cm} \cdot \text{s}^{-1}$ around Cape Point and over Rocky Bank. Together these observations and modelling studies indicate that tidal currents in False Bay are relatively weak, are modulated by the local bathymetry, and can be intensified near constriction points and shallow waters.

Beyond tidal forcing, current variability in the bay also reflects other oscillatory processes, the most prominent of which is inertial motion. Inertial motion is a significant and regular variation in the flow of currents caused by the rotation of the Earth. The inertial period is time that it takes a fluid parcel to complete one inertial oscillation. Inertial currents are generally considered to be of secondary importance when compared to wind and tidal forcing (Wainman, Polito and Nelson, 1987; de Vos, 2022).

2.6 DENSITY STRUCTURE

Density dynamics in False Bay are driven by temperature, with weak contributions from salinity (Gründlingh, 1992). Temperature variability is driven mainly by wind through upwelling and advection of cold water, while solar heating provides a secondary influence, particularly in the shallow northern and north-eastern regions (Atkins, 1970a; Wainman, Polito and Nelson, 1987; Gründlingh, 1992).

Wind-driven upwelling is a dominant feature on the north-west side of headlands throughout the region, particularly during strong south-easterly winds (Largier et al., 1992). The most notable upwelling occurs north-west of Cape Hangklip, and to a lesser extent Gordon's Bay (Atkins, 1970a; Wainman, Polito and Nelson, 1987; Coleman, 2019). Upwelling events can extend up to 20 km east of Cape Hangklip, supplying cold, nutrient-rich water to the interior of the bay (Gründlingh, 1992). In contrast, slack or northerly winds allow warm surface waters to subside along the western coastline leading to warming events of $\sim 6^\circ\text{C}$ at Cape Point and Seal Island (Wainman, Polito and Nelson, 1987).

Seasonal variability in the **thermal structure** is clear. During summer (DJF), False Bay is strongly stratified, with a distinct thermocline and high vertical temperature gradients, particularly in the east where stratification is most intense (Gründlingh, 1992; Dufois and Rouault, 2012). Summer temperature differences of $5 - 9^\circ\text{C}$ are expected between the surface and 50 m depth (Atkins, 1970a). During winter (JJA), the bay is typically well-mixed and cold throughout (Atkins, 1970a; Wainman, Polito and Nelson, 1987; Gründlingh, Hunter and Potgieter, 1989).

Modelling studies confirm the influence of circulation on thermal structure. Nicholson (2011) used the Regional Oceanic Modelling System (ROMS) with tidal and uniform wind forcing to investigate the seasonal stratification in the bay. Their results showed that the bathymetry influences the thermal structure: during

summer surface and bottom flows act independently (are decoupled), with stronger cyclonic circulation at the surface and maximum mean summer velocities around $0.1 \text{ m} \cdot \text{s}^{-1}$. In winter, the water column is well mixed, and flow is weaker and vertically uniform. This is supported by historical observations (Atkins, 1970a; Wainman, Polito and Nelson, 1987; Gründlingh, Hunter and Potgieter, 1989).

Rocky Bank emerges as a key thermal boundary and hydrodynamic modelling indicates that it separates warmer, western waters from colder, eastern waters (Coleman, 2019). Bottom waters east of Rocky Bank are consistently (under well-mixed and stratified conditions) $\sim 1\text{-}2^\circ\text{C}$ colder than to its west (Coleman, 2019). Under stratified summer conditions, north-westerly winds can further advect cold offshore water into the centre of the bay, reinforcing this east-west thermal gradient.

2.7 CIRCULATION

Four main surface circulation patterns have been observed in False Bay since the early 1970s. These vary with wind, tide and local bathymetry. The first descriptions by Atkins (1970b) indicate a dominant bimodal circulation dependent on the prevailing wind regime. During weak winds tidal and inertial currents become important. The influence of wave-driven currents is thought to be most important in the shallow regions, especially in the northern sector. Wind-driven currents dominate the deeper regions of the bay. The following sections describe the circulation patterns driven by south-easterly winds, north-westerly winds, and wave forcing.

South-easterly driven circulation

South-easterly winds typically induce a cyclonic (clockwise in the Southern Hemisphere) circulation throughout False Bay (Fig. 9). A wind shadow in the lee of the Helderberg Mountains allows an anticyclonic circulation to develop near Gordon's Bay (Atkins, 1970b; Taljaard, van Ballegooyen and Morant, 2000; Coleman, 2019). This pattern is mostly observed during summer months when south-easterly winds prevail and has been observed repeatedly (Atkins, 1970b; Wainman, Polito and Nelson, 1987; Gründlingh, Hunter and Potgieter, 1989), and modelled (Van Foreest and Jury, 1985; Nicholson, 2011; Jacobson, 2014; Coleman, 2019; de Vos, 2022).

The clockwise motion is partly established by the bifurcation of a strong west-north-westward flow at the mouth of the bay near Cape Point, which drives an equatorward current along the western shoreline (Isaac, 1937; Atkins, 1970b; Gründlingh, Hunter and Potgieter, 1989; Largier *et al.*, 1992; Boyd *et al.*, 2014). Cyclonic circulation can persist under calm or weaker north-westerly winds, likely due to the contributions of wave-driven currents along the northern shoreline and density structures set up prior strong south-easterly winds (Atkins, 1970a; CSIR, 1982; Jacobson, 2014).

Modelled current magnitudes are typically $\leq 0.1 \text{ m} \cdot \text{s}^{-1}$ and $\leq 0.05 \text{ m} \cdot \text{s}^{-1}$ at the surface and seabed respectively (Coleman, 2019). The decoupling of surface and bottom flows is consistent with observations (Wainman, Polito and Nelson, 1987; Gründlingh, Hunter and Potgieter, 1989). Cyclonic circulation drives offshore advection of nearshore waters near Cape Hangklip and the intrusion of cold offshore waters into the bay near Cape Point (Coleman, 2019).

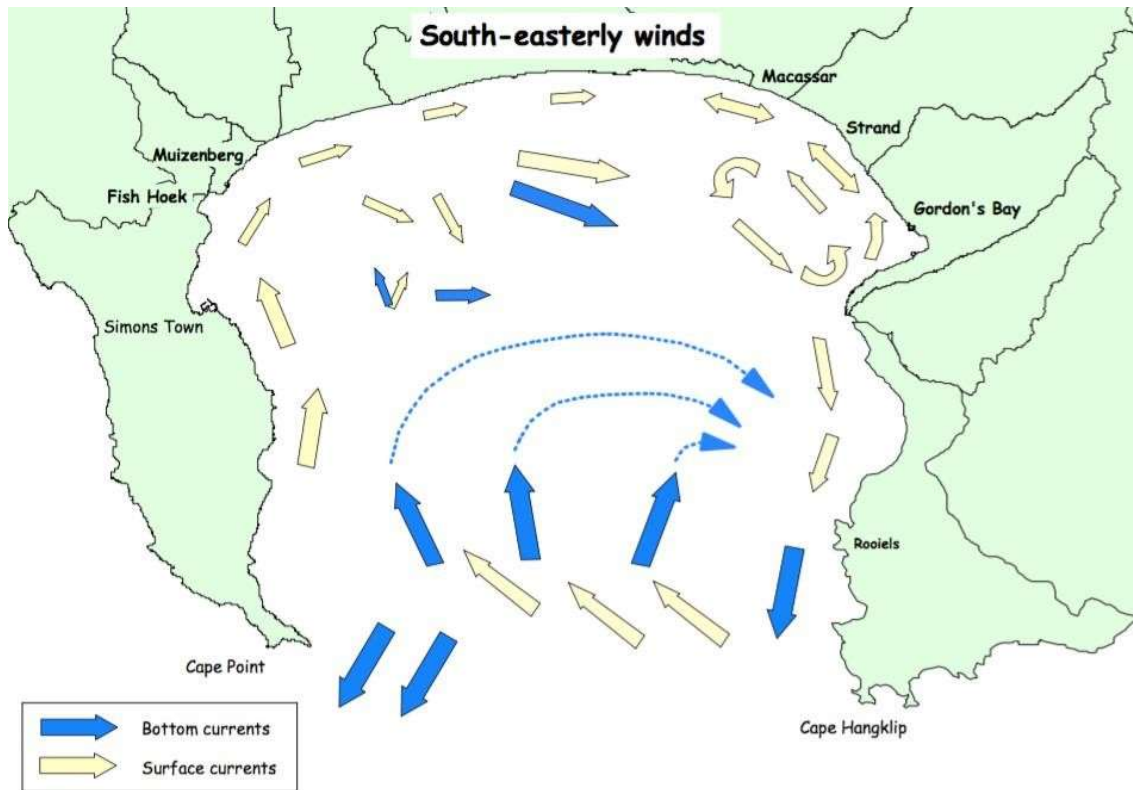


Figure 9) Schematic of the surface flow and deep-water flow in False Bay under southeasterly wind conditions, inferred from previous observational studies from Taljaard et al. (2000). The dotted arrows indicate weak bottom currents.

North-westerly driven circulation

Under north-westerly winds, observations indicate an anticyclonic (anti-clockwise) circulation (Fig. 10) in False Bay (Atkins, 1970b; CSIR, 1982; Wainman, Polito and Nelson, 1987; Gründlingh, Hunter and Potgieter, 1989). North-westerly winds drive an east-north-eastward current near the bay mouth, which is deflected equatorward along the eastern shore, forming a cyclonic gyre near Gordon's Bay (Atkins, 1970b; Wainman, Polito and Nelson, 1987). However the correlation between north-westerly winds and current direction is weaker than for south-easterly winds (Taljaard, van Ballegooyen and Morant, 2000).

Hydrodynamical modelling using ROMS shows that north-westerly winds do not drive the observed anticyclonic circulation (Coleman, 2019). Instead, the model predicts a spatially uniform current field, reflecting the less complex wind field over the bay during these events. Surface currents in deeper waters generally flow southeast at $\sim 0.3 \text{ m} \cdot \text{s}^{-1}$, accelerating up to $0.45 \text{ m} \cdot \text{s}^{-1}$ around Cape Point, Cape Hangklip and along the eastern shoreline. Out-of-bay surface water movement induces bottom currents that advect deep water from the bay entrance toward the centre (Nicholson, 2011; Coleman, 2019). Bottom currents range from $0.05 - 0.10 \text{ m} \cdot \text{s}^{-1}$ in the centre of the bay, but accelerate to approximately $0.30 \text{ m} \cdot \text{s}^{-1}$ around headlands and over Rocky Bank (Coleman, 2019). Recent studies also show that northerly to north-

north-westerly winds promote the development of bottom return currents and vertical shear, and can generate anticyclonic gyres throughout the water column (de Vos, 2022).

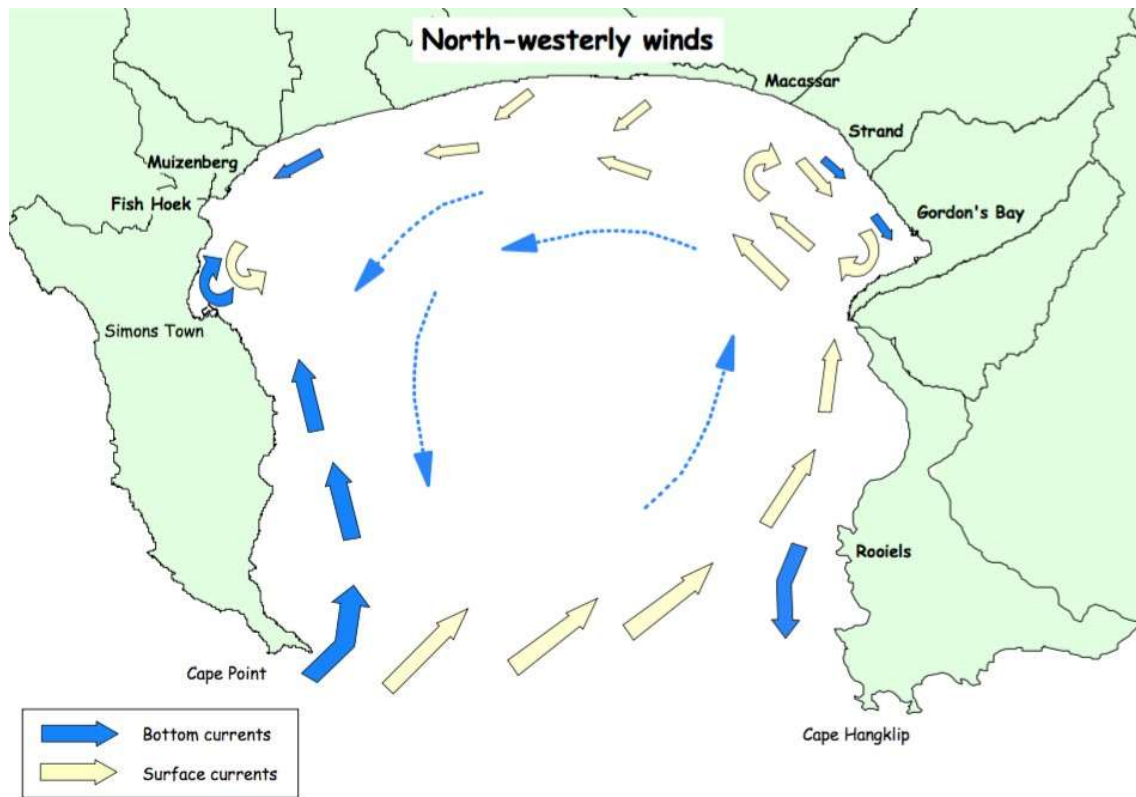


Figure 10) Schematic of the surface flow and deep-water flow in False Bay under north westerly wind conditions, inferred from previous observational studies from Taljaard et al. (2000). The dotted arrows indicate weak bottom currents.

Wave-driven currents are mostly confined to shallow waters along the northern and eastern shores, which have wide surf zones over sandy beaches (CSIR, 1982; Fourie et al., 2015; Salonen, 2019). The direction and magnitude of these currents are largely governed by the angle of obliquely incident waves and wave setup (de Vos, 2022).

Overall, the circulation of False Bay is highly dynamic, alternating with wind regimes, tides, inertial motions, and wave driven processes. Patterns vary on sub-seasonal to decadal time scales, reflecting the complex interplay of bathymetry, stratification, and atmospheric forcing (Dufois and Rouault, 2012).

3 METHODS

3.1 CURRENTS

The data used in this study (Table 1) were obtained through Professor Marcello Vichi and sourced from various stakeholders. The False Bay acoustic Doppler current profiler (ADCP) data were provided by the Department of Oceanography at the University of Cape Town (UCT), the Council for Scientific and Industrial Research (CSIR), the South African Environmental Observation Network (SAEON), and the Institute for Maritime Technology (IMT). The Research Diving Unit at UCT is also acknowledged for their role in the deployment and recovery of the ADCP instruments.

The original metadata accompanying the ADCP deployments were incomplete, contained several inconsistencies, and required verification. Deployment log sheets were examined and cross-checked against the metadata embedded in the raw files. Deployment locations were confirmed using GPS coordinates recorded by the survey vessel. Each deployment originally followed a unique naming convention, which made data management challenging. To standardise the dataset, all raw files were renamed according to a consistent format: `user_location_instrument-type_yyyyymmdd-start_yyyyymmdd-end_deployment-ID`. Each raw dataset was paired with a corresponding CSV file containing complete and verified deployment metadata, which was later used during data processing.

The ADCP records velocity referenced to magnetic directions, which change over time. To simplify interpretation, these measurements are rotated to true geographic directions using the magnetic declination corresponding to the deployment period. Magnetic declinations for each ADCP deployment were calculated using the `oce` R package (version 1.8.-4; Kelley and Richards, 2025). Deployment metadata, including start and end times as well as latitude and longitude, were read from a CSV file. The magnetic declination was calculated at the midpoint time of each deployment. Timestamps were converted to Coordinated Universal Time (UTC) for compatibility with the `oce magneticField()` function. The function was then used to estimate the magnetic field parameters at each deployment location and midpoint time, from which magnetic declination values were extracted. Declinations were expressed in decimal degrees and rounded to six significant figures for consistency (Table 1).

Table 1) Overview of ADCP deployment metadata, showing deployment identifiers, coordinates and time spans. Magnetic declination values were calculated for each deployment using the midpoint time as representative of the deployment period.

Deployment ID	Location		Time (dd mm yyyy hh mm ss) SAST			Magnetic Declination
	Latitude	Longitude	From	To		
Gordon's Bay 1	-34.1217	18.7735	20 05 2015 08 00 00	09 08 2015 00 00 00	-25.2289	
Gordon's Bay 3	-34.1217	18.7735	03 12 2015 07 00 00	04 03 2016 12 40 00	-25.2856	
Gordon's Bay 4	-34.1217	18.7735	09 03 2016 07 00 00	27 06 2016 11 40 00	-25.3152	
Kogel Bay 1	-34.2315	18.8196	11 02 2014 09 00 00	17 04 2014 14 20 00	-25.2107	
Kogel Bay 2	-34.2315	18.8196	16 05 2014 08 00 00	23 07 2014 15 20 00	-25.2377	
Kogel Bay 3	-34.2315	18.8196	20 05 2015 08 00 00	13 08 2015 09 20 00	-25.3443	
Kogel Bay 4	-34.2315	18.8196	21 08 2015 08 00 00	21 11 2015 00 00 00	-25.3718	
Kogel Bay 5	-34.2315	18.8196	03 12 2015 07 00 00	07 03 2016 08 20 00	-25.4016	
Kogel Bay 6	-34.2315	18.8196	09 03 2016 07 00 00	22 06 2016 15 40 00	-25.4305	
Kogel Bay 7	-34.2315	18.8196	23 06 2016 07 00 00	20 09 2016 09 40 00	-25.4582	
Kogel Bay 8	-34.2315	18.8196	18 10 2016 07 00 00	31 01 2017 15 30 00	-25.4936	
Kogel Bay 9	-34.2315	18.8196	07 02 2017 07 00 00	24 05 2017 13 00 00	-25.5253	

The primary goal was to process data from Teledyne RDI Workhorse ADCPs. A number of open-source software solutions were identified and evaluated based on their functionality (Table 2), with emphasis on raw data reading, processing routines including quality control, visualisation, and export to NetCDF. **Pycurrents ADCP processing** (hereafter referred to as *pycurrents*) was selected due to its extensive processing and plotting capabilities, which are described in following sections (Hana Hourston *et al.*, 2023).

A recurring issue arose when reading in raw binary data (.000), as many software options were unable to parse it. This was resolved by converting the binary files to ping data format (.pd0) using **Velocity Tools** (Teledyne RD Instruments, 2018). During this process, a bug in Velocity Tools caused the embedded frequency metadata to double from 614 kHz to 1228 kHz. Teledyne engineers confirmed that the bug is benign but currently do not plan to fix it. After the conversion to .pd0, the data could be correctly parsed by *pycurrents* using a workaround that involved labelling the data as originating from a Sentinel V ADCP. Consequently, the processed NetCDF datasets carry this incorrect metadata. The validity of the underlying data was confirmed by cross-checking against datasets originally processed with the Teledyne's proprietary software.

Table 2) Comparison of open-source software options for Teledyne RDI workhorse ADCP data processing. Key functionalities assessed include data reading, processing, quality control, and visualisation features.

Name	Author/s	Language	Data Reading	Data Processing	Quality Control	Visualisation
pyadps	(v0.2.0; Amol Prakash, 2025)	Python	✓	✓	✓	✓
pycurrents_ADCP_proces sing	(v1.0.1;Hana Hourston et al., 2023)	Python	✓	✓	✓	✓
ADCPy	(v1.2.0;Marinna Martini, 2020)	Python	✓	✗	✗	✗
adcpreader	(v0.2.1;Lucas Merkelbach, 2017)	Python	✓	✓	✓	✗
Marine and Hydrokinetic Toolkit (MHKit)	(v0.9.0; Andrew Simms et al., 2025)	Python/MA TLAB	✓	✓	✓	✓
mADCP	(Gunnar Voet, 2015)	MATLAB	✓	✓	✓	✗
adcptools	(v1.0; Bart Vermeulen, 2021)	MATLAB	✓	✓	✓	✗
Integrated Marine Observing System (IMOS)	(v2.6.15; AODN, 2019)	MATLAB	✓	✓	✓	✗
oce	(v 1.8.-4; Kelley and Richards, 2025)	R	✓	✓	✗	✓

The *pycurrents* pipeline automates the processing of raw ADCP ping data (.pd0). It performed sequential Level 1 and Level 2 processing, and output self-describing L0, L1 and L2 NetCDF datasets along with a standardised set of plots (Fig. 11).

During L1 processing, metadata were read from a user-created CSV file containing deployment information, which was then used to process instrument, geographic, orientation, and deployment details. Raw data were ingested, and key variables were extracted:

- Fixed Leader: system configuration data
- Velocity: current velocity in beam coordinates
- Amplitude: backscatter intensity from each beam
- Correlation: signal correlation quality
- Percent Good: data quality metrics

Velocity data were transformed from beam coordinates to Earth coordinates (East-North-Up), after which user-specified magnetic declinations from the metadata were applied to rotate magnetic velocities to true geographic velocities. Instrument time was converted to Coordinated Universal Time (UTC). Quality control was performed following CF-1.7 conventions and using the SeaDataNet flagging scheme from the British Oceanographic Data Centre (BODC), with flag definitions provided in the Appendix. Instrument depth was

validated against pressure measurements, and negative pressure values were flagged as bad. All data were initially flagged as unprocessed, and ensembles collected outside of the deployment period were flagged as bad.

Several derived variables were calculated (full list in Appendix), and variables were renamed and organised according to CF conventions before creating the L1 NetCDF file. L2 processing applied additional flags for bins affected by surface contamination (indicated by increased backscatter) and negative pressure values. A detailed breakdown of processing scripts and functions is available in the Appendix.

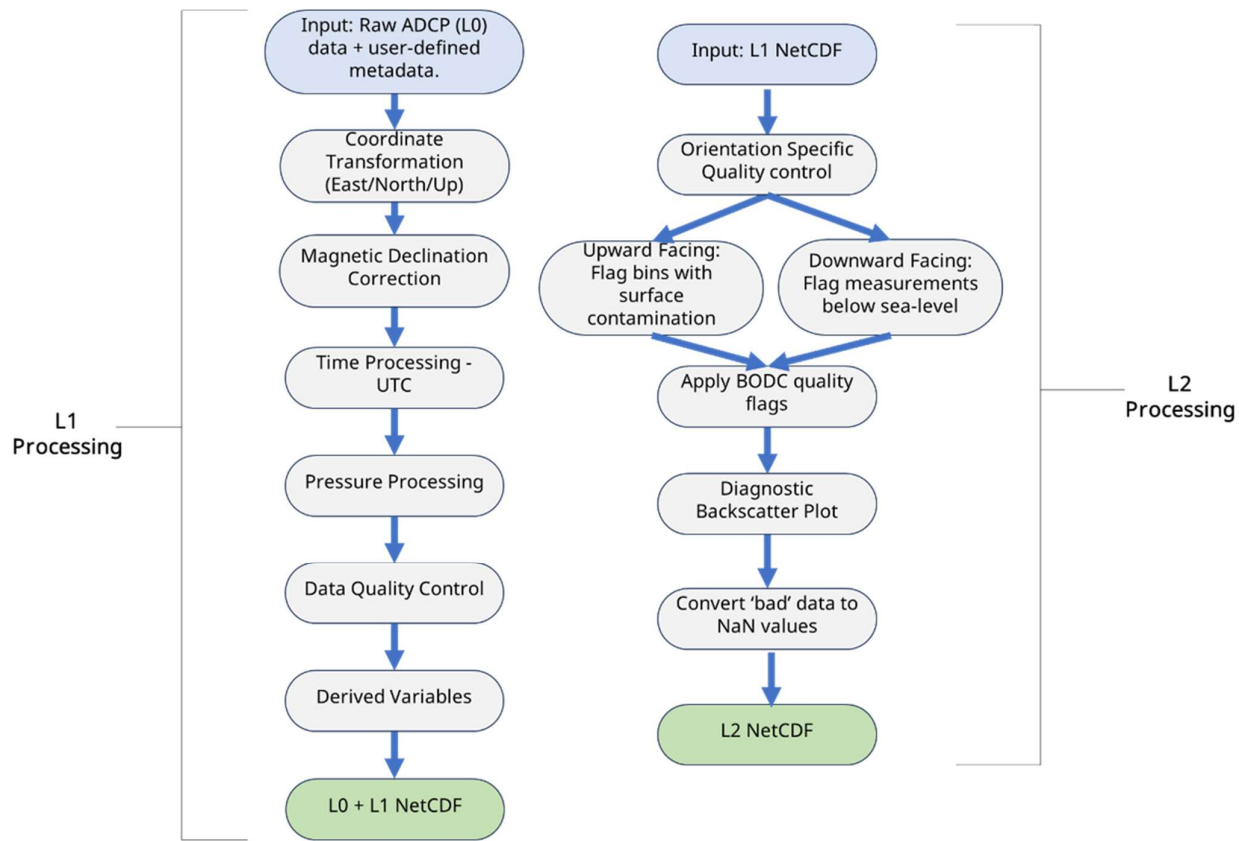


Figure 11 Flow diagram illustrating the pycurrents ADCP processing pipeline. Raw ping data (.pd0) serve as input and undergo Level 1 (L1) and Level 2 (L2) processing. The pipeline produces self-describing NetCDF files and a standardised set of plots.

The **standardised plot set** generated by the pycurrents processing pipeline includes several diagnostic and visualisation tools with additional processing capabilities, described below.

Magnetic velocities were rotated by the user-specified magnetic declination to produce true north and east velocities. **Depth-time plots** were generated for both components. True velocities were aligned with the computed mean alongshore axis to produce alongshore and cross-shore velocity depth-time plots. The mean alongshore axis corresponds to the direction of maximum velocity variance, determined automatically using principal components analysis (PCA). Alternatively, a user-defined alongshore angle can be specified for plotting. By convention, this angle is measured in degrees counterclockwise from east, although it is subject to a 180° ambiguity.

For this study, the alongshore angle was taken as the mean of angles calculated from multiple deployments at the same location – three at Gordon’s Bay and seven at Kogel Bay. This provided a representative estimate of the observed alongshore orientation.

Velocity quiver plots were generated to display current speed and direction as blue vectors at three depth layers – surface, middle and bottom – corresponding to bins defined during ADCP configuration. Grey shading above the velocity axis indicates absolute current magnitude.

Several **low-pass filters** can be applied within the script to dampen oscillations shorter than the filter window (high-frequency processes) while retaining oscillations longer than the filter window (low-frequency processes). A Godin low-pass filter was applied to the data. This triple running-median filter, designed for tidal analysis, effectively removes variability on time scales shorter than approximately 2-3 days. Variability with periods longer than about three days remains largely preserved. The remaining non-tidal variability near this cutoff is substantially attenuated. Further details on the Godin filter are provided by Thomson and Emery (2024). In addition, a user-defined running-median filter window can be specified, allowing targeted analysis of specific frequency bands and processes.

Spectral analysis partitions the variance of a time series as a function of frequency. **Rotary spectral analysis** extends this concept by decomposing the velocity vector at each frequency into clockwise (CW) and counterclockwise (CCW) rotating components. This separation reveals important aspects of the wave field and is particularly useful for investigating currents influenced by abrupt topography, wind-generated inertial motions, diurnal continental shelf waves, and other forms of narrow-band oscillatory flow.

The rotary spectra presented in this study were computed using Welch's Method; readers are referred to Thomson and Emery (2024) for methodological details. Many rotary properties, including power spectral density, are invariant under coordinate rotation, meaning that local steering effects due to coastline or bathymetry do not affect the analysis. In the Southern Hemisphere, inertial motions are almost entirely counterclockwise-rotary, and thus the clockwise component can typically be ignored for most applications.

Tidal analyses produced tidal ellipse profiles for each specified tidal constituent. Each ellipse represents the combined effect of the CW and CCW rotary velocity components at that constituent's frequency. The orientation (tilt) of the ellipse, measured relative to the eastward horizontal axis, indicates the rotation of the major axis counterclockwise from east. The length of the major axis reflects the magnitude of the tidal oscillation, while the sense of rotation describes the current's rotational direction: a counterclockwise - tilted ellipse corresponds to a counterclockwise rotation of the tidal current, and a clockwise tilt indicates a clockwise rotation.

The processing pipeline was demonstrated using data from two deployments - one near **Gordon's Bay** and one by **Kogel Bay**. Plots for the entirety of each deployment (roughly four months) were generated using the L1 NetCDF datasets. The L2 data from the Gordon's Bay ADCP during January 2016 were used in a case study designed to illustrate some research applications of the high-frequency archival ADCP data reprocessed by the pipeline. Wave data from the same ADCP and time period were also processed, and modelled wind data were incorporated to demonstrate applications in coastal oceanography. An in-depth analysis of physical drivers fall outside the scope of this project.

The two Teledyne RDI Workhorse ADCPs used in this case study were deployed in False Bay (Fig. 12). The first was positioned near Gordon's Bay at 34.1217° S, 18.7735° E in approximately 24 m of water, and the second near Kogel Bay at 34.2315° S, 18.8196° in roughly 23 m of water. The Gordon's Bay deployment ran from 03 December 2015 to 04 March 2016, and the Kogel Bay deployment from 03 December to 07 March 2016. Magnetic declinations at the deployment midpoints were -25.2289 ° and -25.4016°, respectively. Both instruments operated at 614 kHz and recorded data in 30 depth cells (1 m each), with ensemble averages collected at 20-minute intervals. Leading and trailing ensembles corresponding to deployment and recovery were removed during processing.

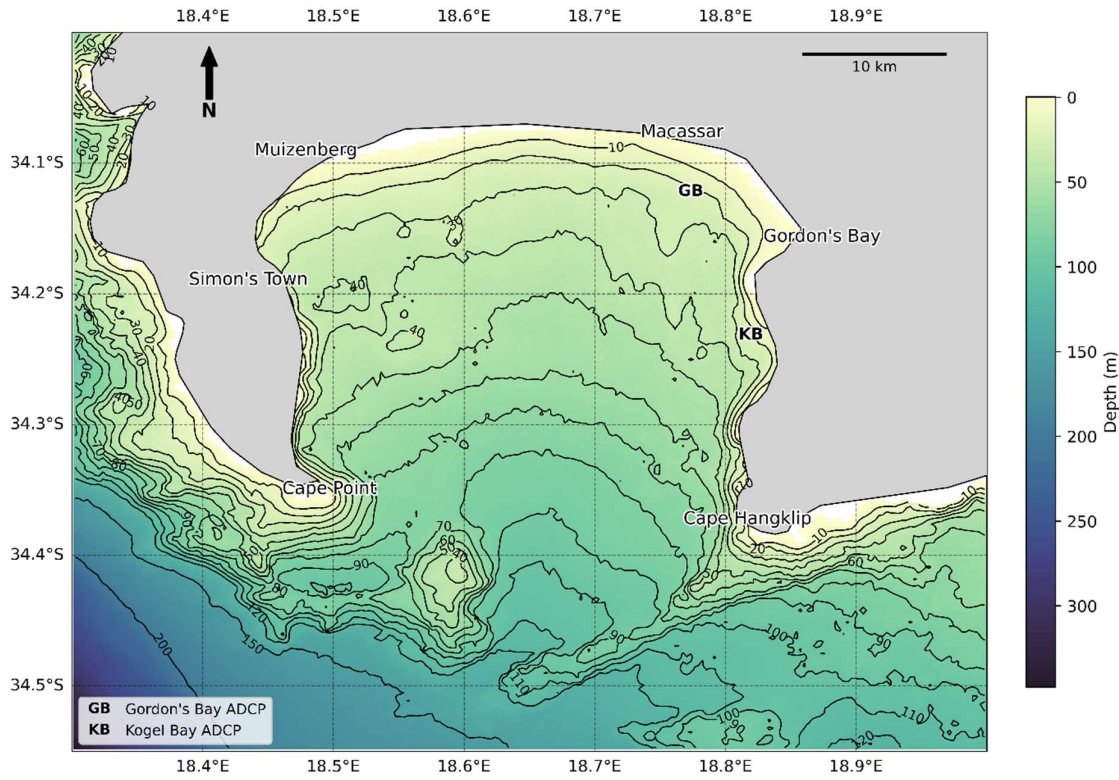


Figure 12) Map of False Bay bathymetry showing ADCP deployment sites near Gordon's Bay and Kogel Bay. Prominent coastal landmarks are also indicated. Bathymetry data from de Wet and Compton (2021).

3.2 WINDS

Wind and wave dynamics in False Bay are strongly influenced by local and regional wind forcing. A reanalysis product combines observational data with model simulations through a process called data assimilation. Two reanalysis wind products were used in this study: the ERA5 global wind reanalysis and the high-resolution Wind Atlas for South Africa 3 (WASA3).

ERA5, the fifth generation atmospheric reanalysis produced by the European Centre for Medium-Range Weather Forecasts (ECMWF), provides global coverage from 1940 to present (Hersbach *et al.*, 2020). The dataset has a horizontal resolution of $0.25^\circ \times 0.25^\circ$, corresponding to approximately $23\text{ km} \times 28\text{ km}$ per grid cell in False Bay, and 137 vertical levels extending up to 0.01 hPa. Despite this vertical detail, the relatively coarse horizontal resolution limits the model's ability to resolve the complex orography surrounding False Bay. In this case study we used the 10 m wind speed and direction.

WASA3 is a high-resolution atmospheric reanalysis product generated using the open-source Weather Research and Forecasting (WRF v3.8.1) model (Lennard *et al.*, 2021). The domain spans the South African Exclusive Economic Zone at a horizontal resolution of $3\text{ km} \times 3\text{ km}$, with half-hourly wind speeds and directions. The vertical grid consists of 61 levels, 20 of which are below 1000 m, offering sufficient resolution to capture the complex orography surrounding False Bay. The lowest available level is 20 m. For this study, wind speeds and directions were adjusted to 10 m above sea level using the World Meteorological Organization (WMO) wind speed correction equation with an upstream roughness length of 0.10 m, representative of low crops and occasional large objects (World Meteorological Organization, 2024). WASA3 has been extensively validated (Hahmann *et al.*, 2021) and applied in a previous study of local wind effects (Daniels *et al.*, 2022).

The ERA5 wind data used in this study were taken from the grid cell closest to the Kogel Bay site (Fig. 13). Fifteen WASA3 grid cells were selected to represent both deployment locations.

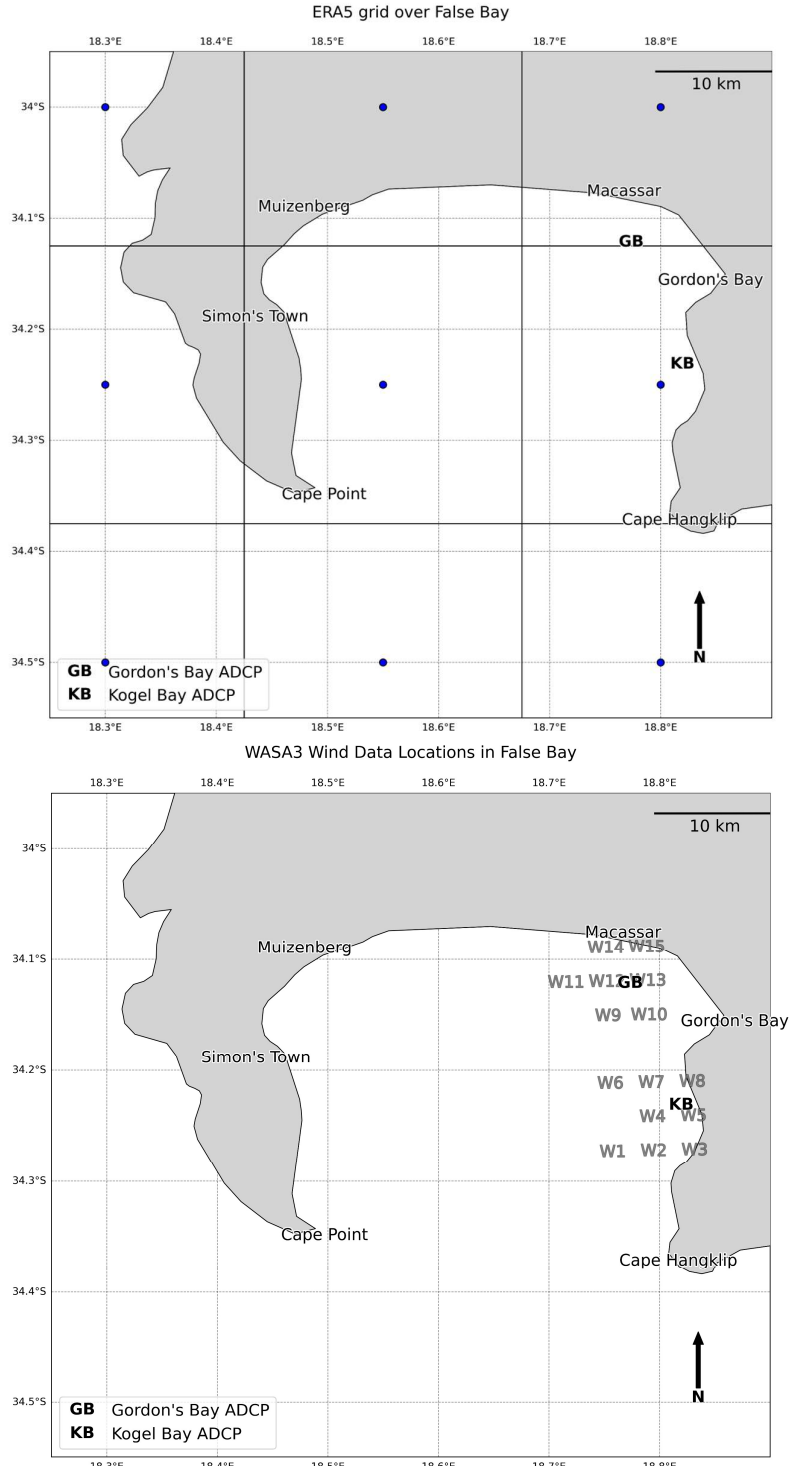


Figure 13) Maps showing ERA5 grid cells (top) and selected WASA3 grid cells (bottom) over False Bay. WASA3 grid cell centres are indicated by labels, which increase sequentially from southwest to northeast.

3.3 WAVES

Waves play a critical role in modulating nearshore circulation by influencing both coastal currents and sediment transport. Wave data from the Gordon's Bay deployment were processed to investigate local wave conditions during the study period. The analysis provided additional context for interpreting current variability and highlighted the limitations of the proprietary software used for wave processing.

Wave data for the Gordon's Bay deployment (03/12/2015 to 04/03/2016) were processed using Teledyne RDI **WavesMon** (v3.08) software. Wave parameters were computed by scaling the directional spectrum with the corresponding non-directional spectra derived from velocity, pressure, and surface track measurements. Orbital velocity-derived spectra were the primary source for wave parameter determination. If these spectra were flagged as invalid, pressure-derived spectra were used, and if those were also invalid, the surface track spectra were used. This hierarchical approach ensures that wave parameters are generated from the best available data while utilising redundant measurements.

Detailed frequency distributions of wave parameters cannot be exported from WavesMon; therefore, the full wave energy spectra for January 2016 are omitted here. However, selected snapshots generated within the software are included for reference.

The main parameters are defined as follows:

- H_s : Significant Wave Height (m).
- T_p : Peak Wave Period (s) — period associated with the largest spectral peak.
- D_p : Peak Wave Direction ($^{\circ}$) — direction at the peak period.
- **Sea and swell parameters:**
 - $T_{p,Sea}$, $D_{p,Sea}$, $H_{s,Sea}$: Peak period, direction, and significant height in the sea portion of the spectrum.
 - $T_{p,Swell}$, $D_{p,Swell}$, $H_{s,Swell}$: Peak period, direction, and significant height in the swell portion of the spectrum.

The sea and swell parameters are separated using a user-defined transition frequency, here set to 0.125 Hz , meaning that waves with periods longer than 8 seconds are classified as swell. The sea parameters correspond to wind-generated waves.

Significant wave height (H_s) is calculated using the frequency domain definition (Holthuijsen, 2007):

$$H_s = 4\sqrt{m_0},$$

where m_0 is the zeroth moment of the variance spectrum.

4 RESULTS AND DISCUSSION

4.1 GORDON'S BAY AND KOGEL BAY

The processing pipeline successfully handled raw ADCP data from ten deployments – three at Gordon's Bay (May 2015 -June 2017) and seven near Kogel Bay (May 2015 -May 2017). For each deployment, three self-describing NetCDF files were produced (L0, L1 and L2) containing georeferenced velocity, error, and backscatter data, as well as pressure and temperature records. Standardised plots were generated from the L1 and L2 datasets for each deployment. Results from Gordon's Bay Deployment 3 and Kogel Bay Deployment 5 (both spanning December 2015 to March 2016) are presented here to demonstrate the pipeline's capabilities as in-depth data analysis falls outside the scope of this project.

4.1.1 Velocity Timeseries

The circulation at both deployments was characterised by high variability in both current magnitude and direction (Fig. 14). At the Gordon's Bay deployment, current speeds reached a maximum of 1.23 m s^{-1} , with a mean of $0.13 \pm 0.12 \text{ m s}^{-1}$. The mean current direction was slightly north of east-northeast (63.2° true) but exhibited large variability ($\pm 108.5^\circ$). High-magnitude currents were predominantly oriented northwest, parallel to the local shoreline.

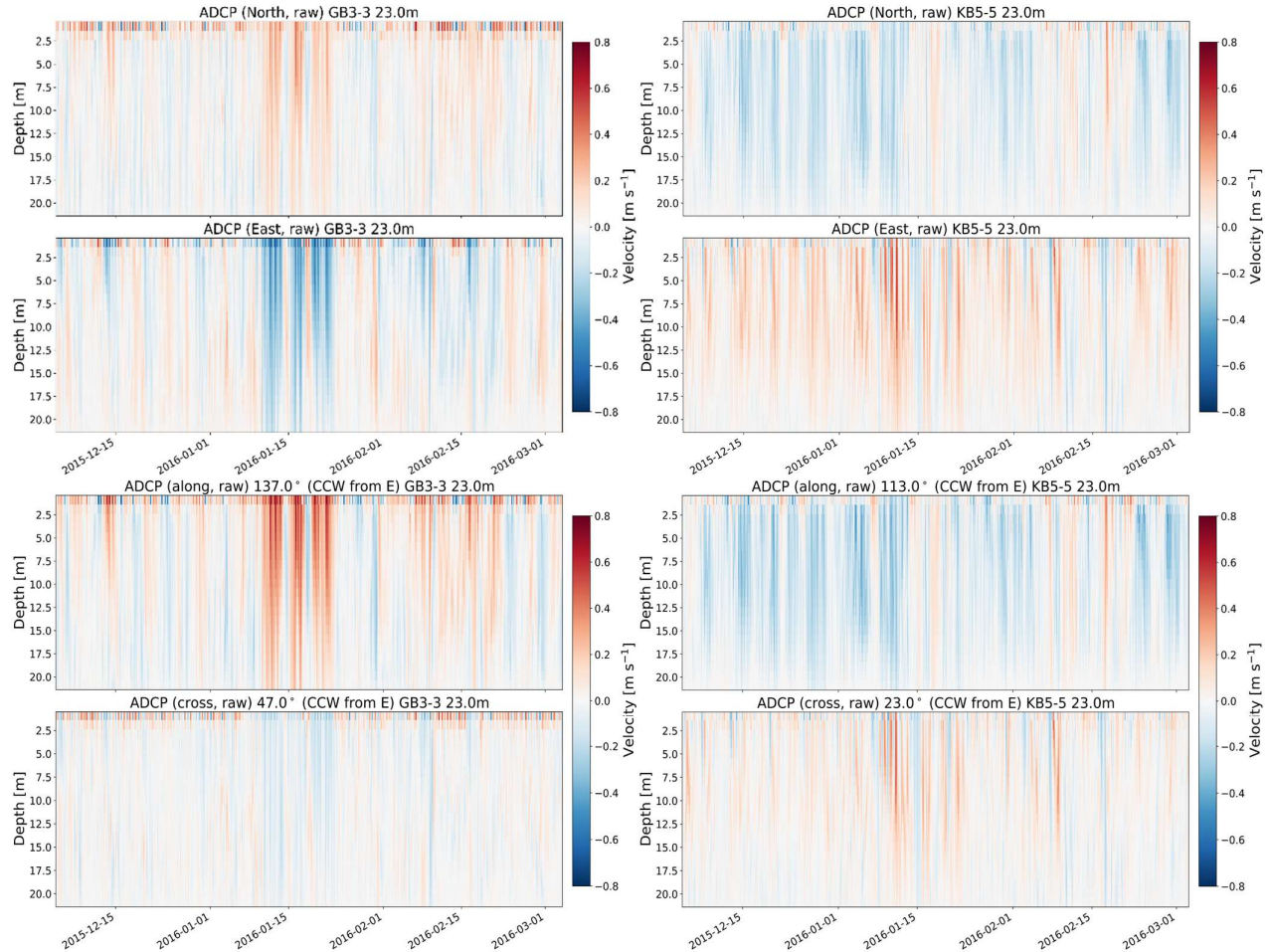


Figure 14) True and alongshore velocity profiles of unfiltered L1 ADCP data from Gordon's Bay D3 (left panels) and Kogel Bay Deployment 5 (right panels). Magnetic velocities were rotated by the local magnetic declination to produce true north-east components (top panels). The along shore and cross-shore velocities (bottom panels) are aligned with the mean alongshore axis determined by PCA.

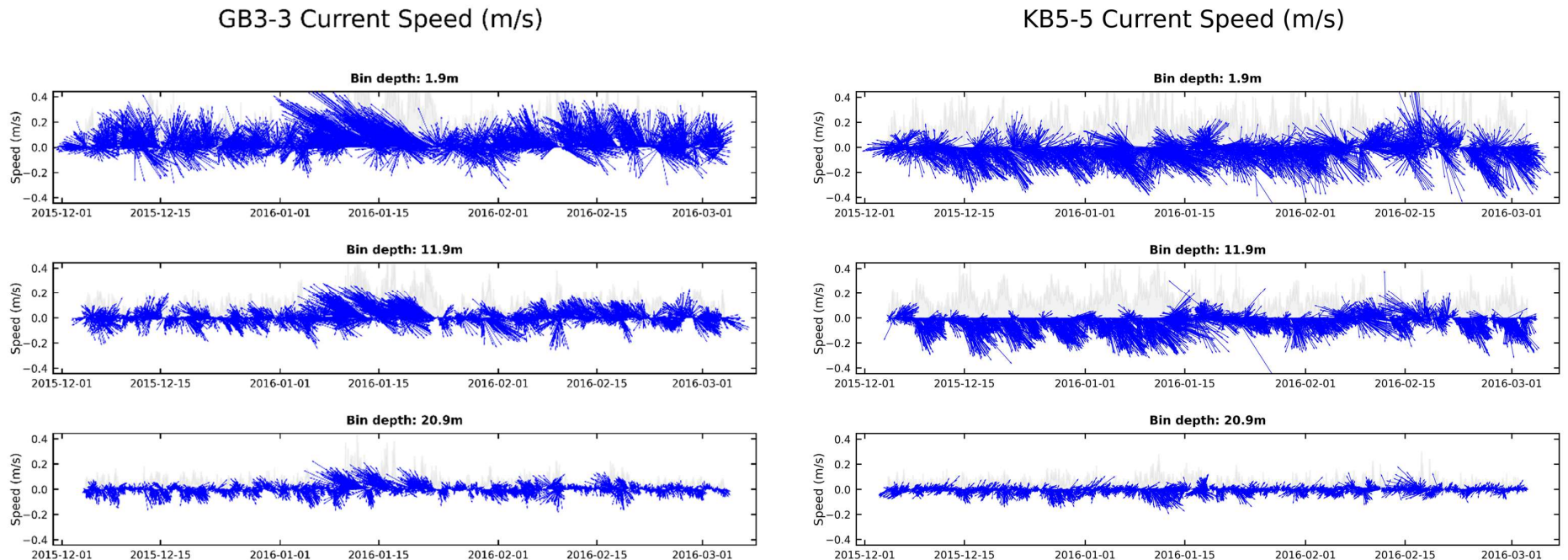


Figure 15) Velocity quiver plots for unfiltered L1 ADCP data from Gordon's Bay D3 (left panels) and Kogel Bay Deployment 5 (right panels). Blue arrows represent current vectors at three depth bins: surface, middle and bottom. Each vector represents a 20 minute ensemble and grey shading above the velocity axis indicates absolute current magnitude.

The circulation at both deployments was characterised by high variability in both current magnitude and direction (Fig. 14). At the Gordon's Bay deployment, current speeds reached a maximum of 1.23 m s^{-1} , with a mean of $0.13 \pm 0.12 \text{ m s}^{-1}$. The mean current direction was slightly north of east-northeast (63.2° true) but exhibited large variability ($\pm 108.5^\circ$). High-magnitude currents were predominantly oriented northwest, parallel to the local shoreline.

Current speeds at the Kogel Bay Deployment reached a maximum of 1.15 m s^{-1} , with a mean of $0.14 \pm 0.11 \text{ m s}^{-1}$. The mean current direction was approximately east-southeast (118.1° true) and similarly variable ($\pm 85.0^\circ$). High-magnitude currents were oriented in the same direction, roughly parallel to the local shoreline.

Across both deployments, current speeds decreased with depth, with the strongest flows near the surface and attenuating towards the seafloor (Fig. 15). Current direction remained largely consistent throughout the water column, suggesting depth-uniform flow during most conditions.

During summer (DJF), the prevailing south-easterly winds typically induce a cyclonic (clockwise) circulation in False Bay, with current magnitudes of $\leq 0.1 \text{ m s}^{-1}$ at the surface and $\leq 0.05 \text{ m s}^{-1}$ near the seafloor (Wainman, Polito and Nelson, 1987; Coleman, 2019). These align well with the observations from the Kogel Bay deployment, where currents followed the expected pattern for the time of year. At the Gordon's Bay deployment, however, the pronounced north-westward flow observed during high-magnitude events has not been previously reported. This feature may indicate the influence of locally forced wind-driven circulation, wave-driven currents operating in the shallow northeastern zone, or a combination of the two. The direction and magnitude of wave-driven currents are governed by the angle of obliquely incident waves and wave setup (CSIR, 1982; Fourie et al., 2015; Salonen, 2019; de Vos, 2022).

4.1.2 Rotary Spectra

The frequency distribution of both clockwise (CW) and counterclockwise (CCW) components of power spectral density (PSD), which represents the distribution of power across frequencies, were broadly similar at both the Gordon's Bay and Kogel Bay deployments (Fig. 16). Lower PSD values occurred at high frequencies and are likely associated with small-scale turbulent processes. Peaks in PSD were found at lower frequencies, with two of these aligning with the principal lunar semi-diurnal (M2) and solar diurnal (S2) tidal frequencies. This does not imply direct tidal forcing; it indicates that PSD is concentrated near these periodicities. The largest PSD peak corresponds to variability on timescales of approximately nine days, likely capturing the influence of passing synoptic weather systems that dominate the regional wind field.

Processes with a diurnal frequency exhibited depth-dependent variations in PSD (Fig. 17). The CW component was strongest near the surface and diminished slightly with depth, consistent with the expected rotation of inertial motions in the Southern Hemisphere (Thomson and Emery, 2024). In contrast, the CCW component showed a strong vertical gradient, suggesting enhanced vertical shear and mixing within the water column. This results from the combined effects of wind, wave and tidal motions that operate at diurnal frequencies.

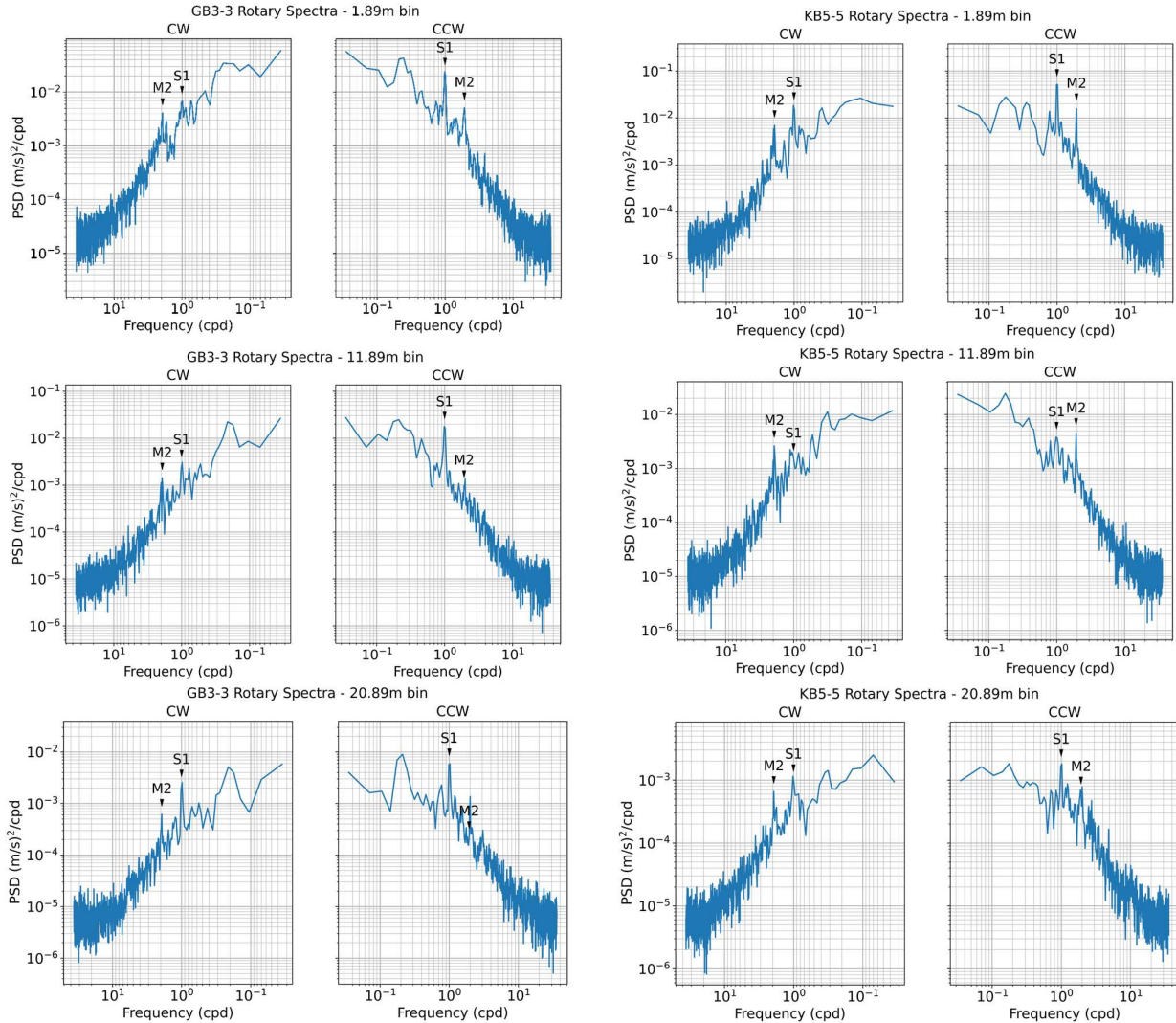


Figure 16) Rotary spectra for unfiltered L1 ADCP data from Gordon's Bay D3 (left panels) and Kogel Bay Deployment 5 (right panels). Subplots show clockwise (negative) and counter-clockwise (positive) components of power spectral density (signal's distribution of power at different frequencies) at surface, middle and bottom depths, plotted against log frequency in cycles per day. M2 and S1 denote the PSD peaks associated with the frequencies of the principal lunar semi-diurnal and solar diurnal tides, respectively.

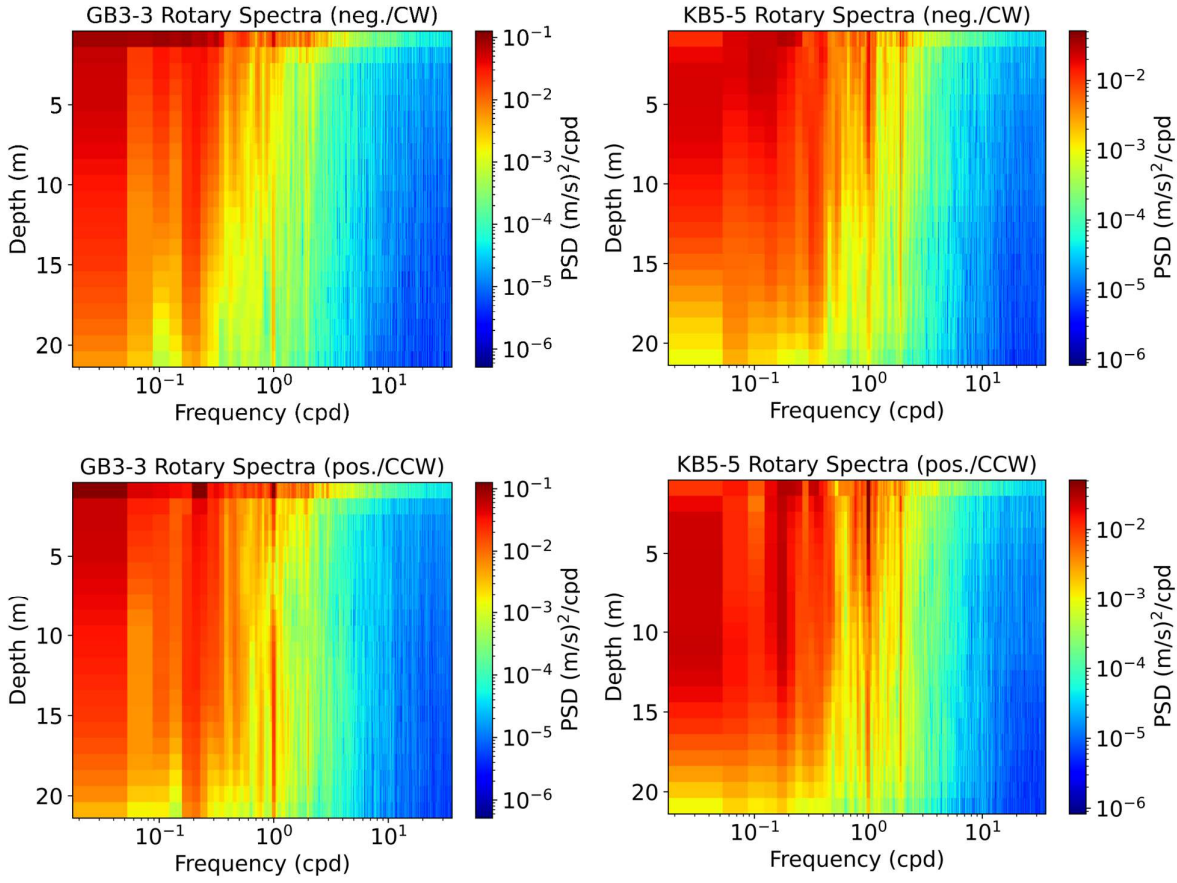


Figure 17) Rotary spectra for unfiltered L1 ADCP data from Gordon's Bay D3 (left panels) and Kogel Bay Deployment 5 (right panels). Subplots show clockwise (negative) and counterclockwise (positive) components of power spectral density, over depth and against log frequency in cycles per day.

4.1.3 Tidal Ellipses

The solar diurnal tidal constituent (S1), with a period of 24 hours, was identified as the dominant tidal constituent at both deployments. This contrasts the findings of Gründlingh et al. (1989), who reported the semi-diurnal tidal constituent (12-hour period) as most significant near the mouth of False Bay. At the Gordon's Bay deployment, tidal flow was generally aligned along a north-northeast to south-southwest direction (in and out of the bay), with mean flow rates below 5 cm s^{-1} . At the Kogel Bay deployment, tidal flow was generally aligned along an east-northeast to west-southwest direction (across the bay), with comparable magnitudes. These flow rates are consistent with those reported by Gründlingh et al. (1989), who observed tidal currents ranging between 2.2 and 3.3 cm s^{-1} . Our observations support the understanding that the tidal currents in False Bay are generally weak but can interact with bathymetric features, leading to local accelerations of up to 25 cm s^{-1} (Coleman, 2019)

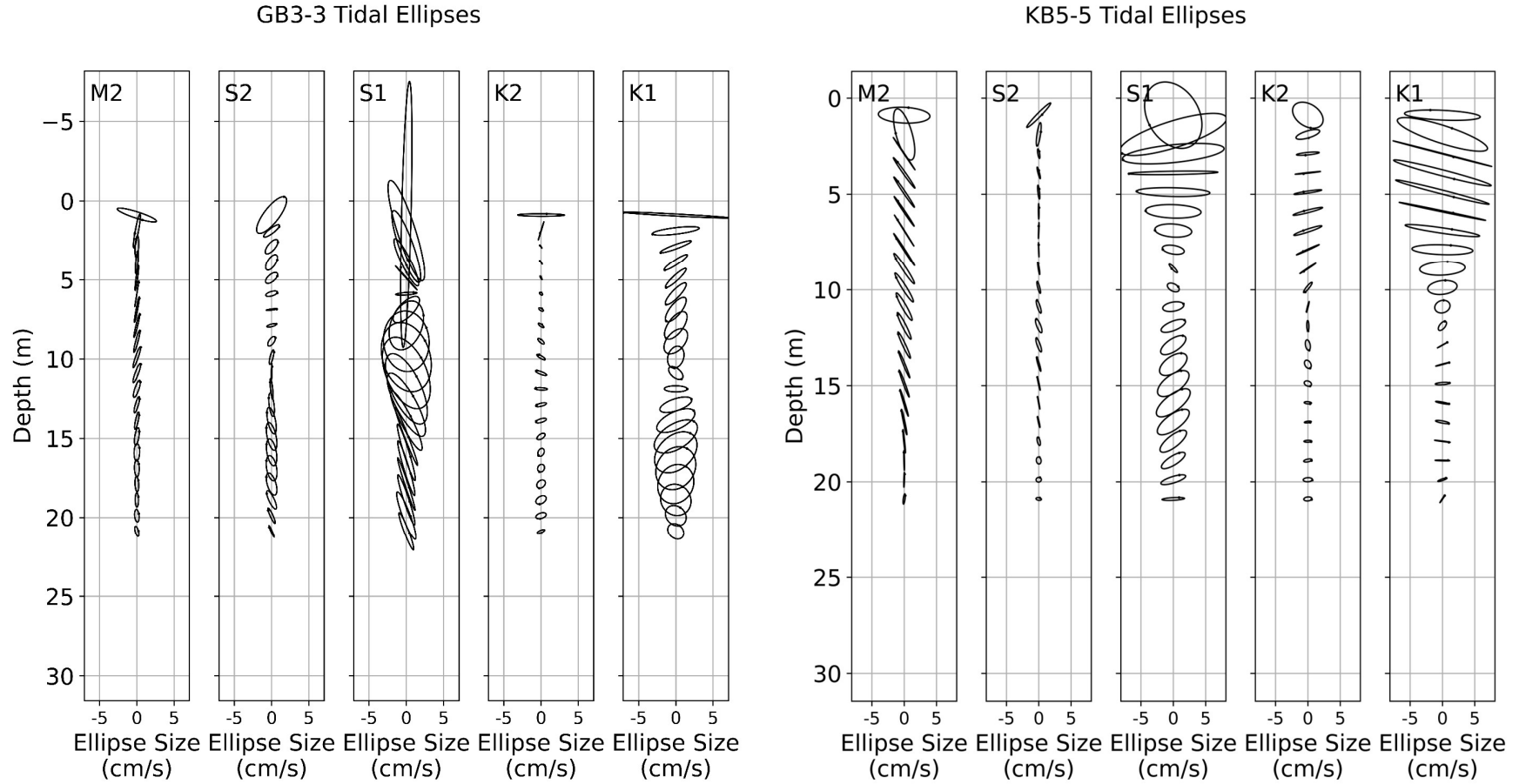


Figure 18) Tidal ellipse profiles for specified tidal constituents for unfiltered L1 ADCP data from Gordon's Bay D3 (left panels) and Kogel Bay Deployment 5 (right panels). Each ellipse represents the combination of clockwise and counterclockwise rotary velocity components at the constituent's frequency. The tilt of the ellipse measured relative to a horizontal line at its centre the rotation of the major axis counterclockwise from east. The length of the major axis reflects the magnitude of the tidal oscillation. A counterclockwise -tilted ellipse corresponds to counterclockwise rotation of the tidal current and vice versa.

4.2 CASE STUDY: JANUARY 2016

Level 2 data from January 2016 were selected to demonstrate the potential research applications of the recovered data. Current and parameters were derived from the raw ADCP measurements using the open-source processing pipeline and proprietary software, respectively. Wind reanalysis data were incorporated to infer the drivers of observed current and wave variability.

We begin by examining the current structure and wind fields at both the Gordon's Bay and Kogel Bay ADCP sites. Winds are shown for each location. We then focus on Gordon's Bay to present diagnostic analyses and wave results, before concluding with a comparison of winds, waves and currents at Gordon's Bay.

4.2.1 Currents

The circulation at both deployments was consistent with the patterns described previously, showing substantial variability in both current magnitude and direction. At Kogel Bay, the flow was more uniform and generally followed the expected clockwise circulation, consistent with the prevailing southeasterly wind regimes typical of austral summer. The mean currents speed was $0.15 \pm 0.11 \text{ m s}^{-1}$, predominantly toward the east-southeast (118.0°) with a high directional spread of 83.1° .

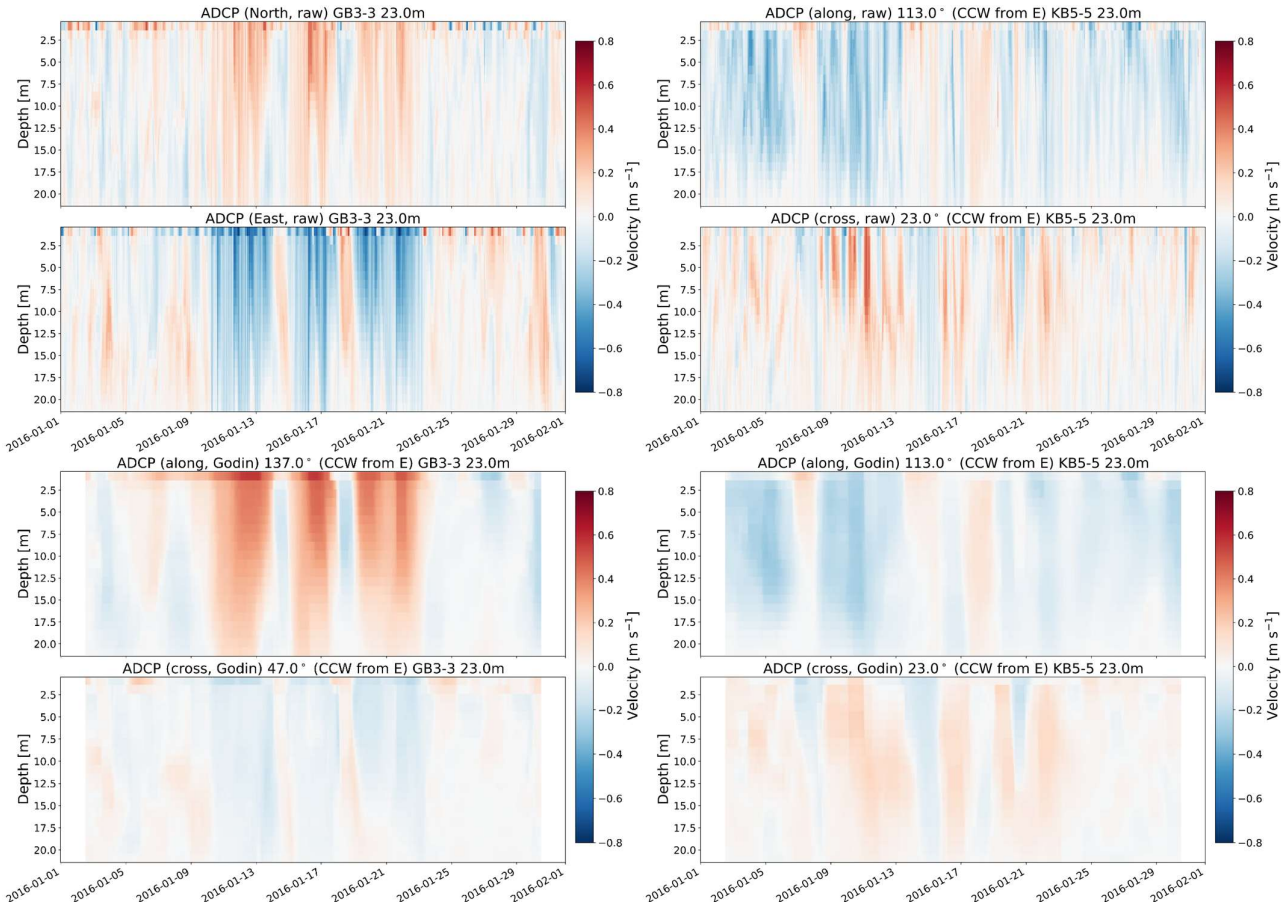


Figure 19) Velocity profiles of unfiltered (top panels) and Godin low-pass filtered (bottom panels) L2 ADCP data from Gordon's Bay D3 (left) and Kogel Bay D5 (right). The alongshore and cross-shore velocities are aligned with the mean alongshore axis determined by PCA.

At Gordon's Bay, the currents were more variable. The mean flow was predominantly clockwise. The mean current speed was $0.16 \pm 0.14 \text{ m s}^{-1}$, oriented toward the northeast (52.1°) with a very high directional spread of 111.1° . The velocity distribution (Fig. 19) reveals a pulsed flow pattern with a median speed of 0.12 m s^{-1} , lower than the mean, indicating frequent calm periods interspersed with strong flow events. During these high-magnitude events, the current direction reverses to counterclockwise. This reversal suggests that local forcing — most likely strong southeasterly winds — may generate a nearshore counter-current along the northeastern shore of the bay.

Although not shown here for brevity, the rotary spectra indicate depth-varying rotational energy at the diurnal frequency, implying strong vertical shear. Large wave events may erode coastal sediments or resuspend sediments from the nearshore zones of Monwabisi and Macassar. Episodic high-shear current events could transport these sediments westward along the northern shore where they can be deposited under calmer local conditions.

Such a mechanism could contribute to the accumulation of sediment in the northwestern corner of False Bay, particularly in sheltered areas such as Muizenberg, Fish Hoek and Simon's Bay. The entire northwestern periphery of the bay experiences recurring sand inundation, especially during summer months (Colenbrander, 2017). This has necessitated extensive management interventions, including mechanical beach lowering and dune restoration. While aeolian transport is likely the dominant driver of sand transport, little is known about the contribution of waterborne sediment transport, beyond evidence that high-magnitude wave events cause shoreline erosion along the northeastern shore (Fourie *et al.*, 2015).

These observations highlight the value of high-frequency current measurements in shallow coastal environments, where short-lived energetic events may dominate sediment transport, shoreline morphology, and mixing.

4.2.2 Wind Reanalysis

4.2.2.1 European Centre for Medium-Range Weather Forecasts (ECMWF) Reanalysis v5 (ERA5)

The variability of both the wind speed and direction from ERA5 was moderate to high, with little variation between grid cells (Fig. 20). The mean hourly wind speed at the ERA5 grid cell near nearest the Kogel Bay deployment site was $7.35 \pm 3.24 \text{ m s}^{-1}$, with a maximum of 17.7 m s^{-1} and a minimum of 0.55 m s^{-1} . Wind directions were highly variable, ranging between south-westerly and southeasterly, with a circular standard deviation of 54.6° (Fig. 21). The mean wind direction was south-southeasterly 166.2° . This apparent homogeneity of the ERA5 wind field is inconsistent with historical observations and recent literature (Wainman, Polito and Nelson, 1987; Gründlingh, Hunter and Potgieter, 1989; Jacobson, 2014; Daniels *et al.*, 2022).

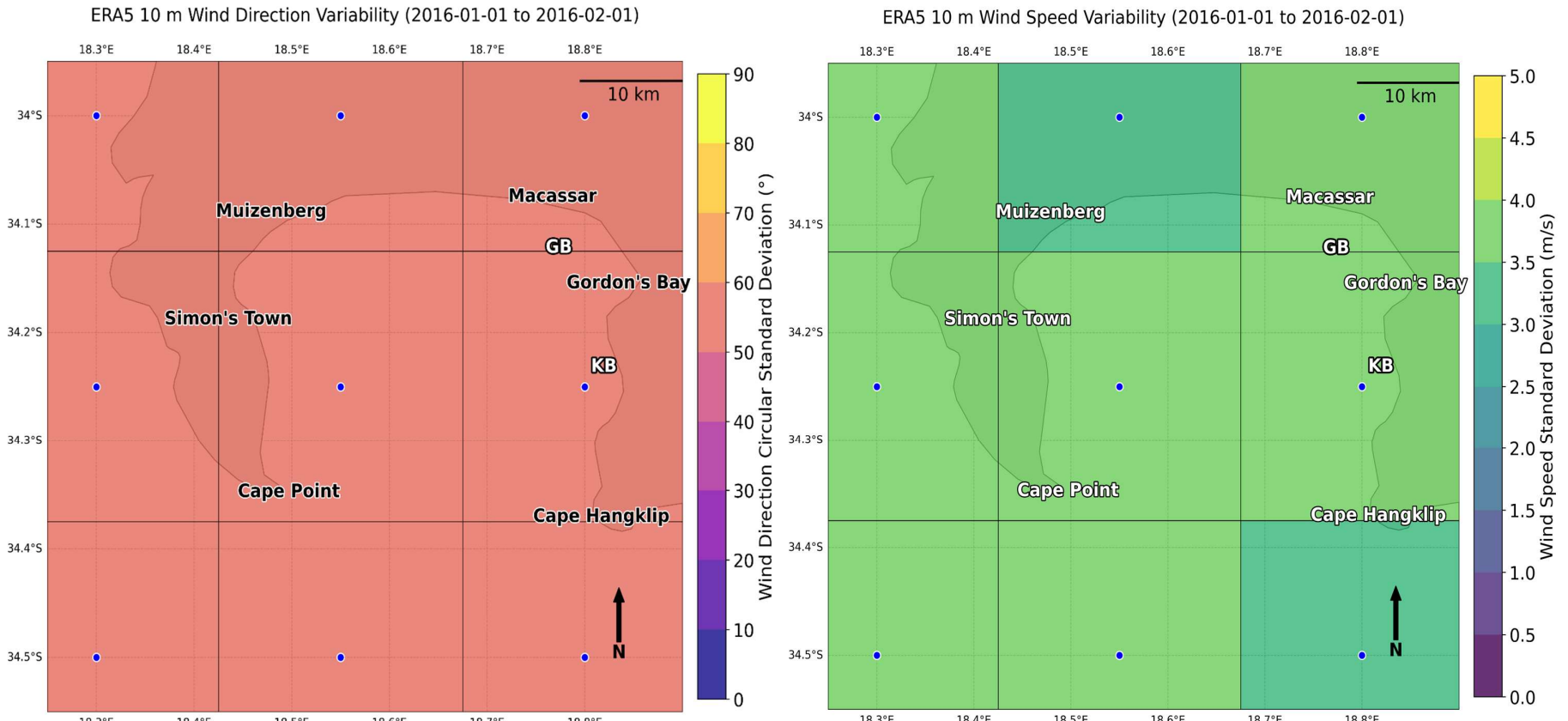


Figure 20) Maps showing ERA5 grid-cell centres (blue dots) over False Bay, including ADCP deployment locations and prominent places. Colours represent the circular standard deviation of wind direction (left) and the standard deviation of wind speed (right) over January 2016.

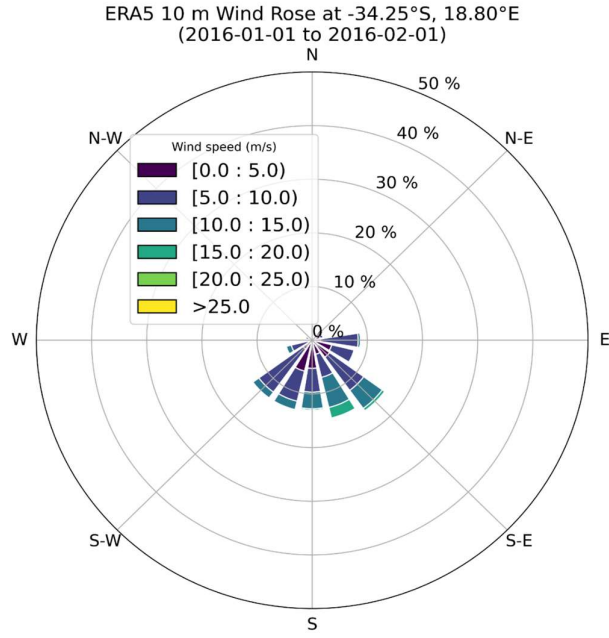


Figure 21) Wind rose (10 m) for the ERA5 grid cell covering both ADCP deployments for January 2016.

4.2.2.2 Wind Atlas for South Africa 3 (WASA3)

WASA3 winds, computed at 20 m, were corrected to a 10 m reference height to match ERA5. This correction reduced the wind speeds by approximately $\sim 27\%$ (Fig. 22), resulting in a mean 10 m wind speed of $7.99 \pm 3.24 \text{ m s}^{-1}$. The mean temporal circular standard deviation across 15 WASA stations was similar to ERA5 (54.2°), with a mean wind direction of south-easterly (127.6°). Wind speed was more variable near the Kogel Bay site, while wind direction showed greater variability at Gordon's Bay (Fig. 23).

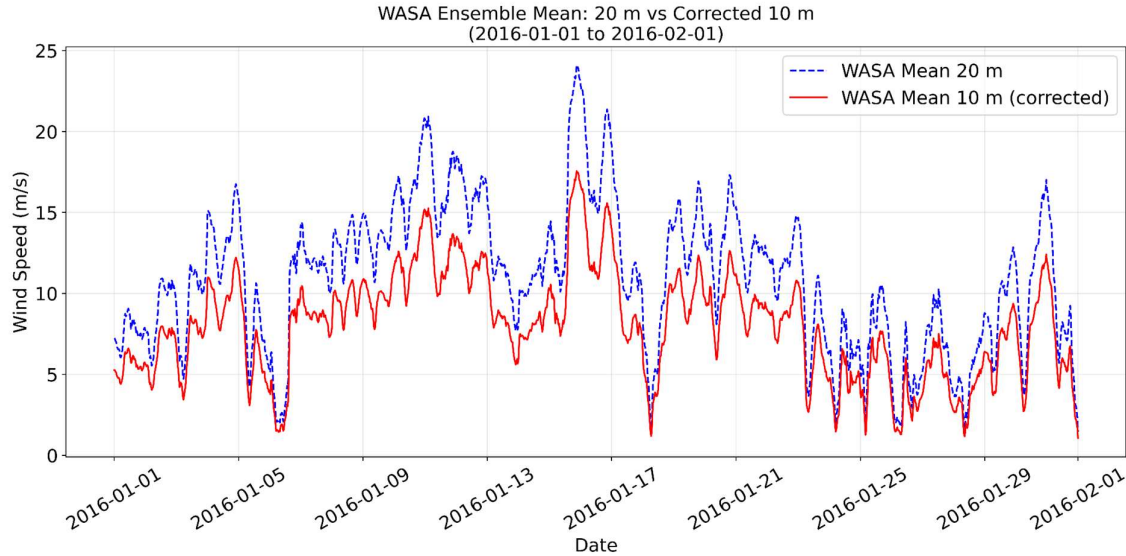


Figure 22) Comparison between the original WASA3 mean wind speed at 10 m (blue dashed line) and the corrected WASA3 mean wind speed at 10 m.

Winds at Kogel Bay exhibited a strong easterly component, whereas Gordon's Bay experienced a stronger east-southeasterly component (Fig. 24). Wind speeds near Gordon's Bay were generally lower throughout the study period, likely reflecting the influence of the Helderberg Mountains, which produce a wind shadow in their lee under shallow southeasterly conditions (Wainman, Polito and Nelson, 1987).

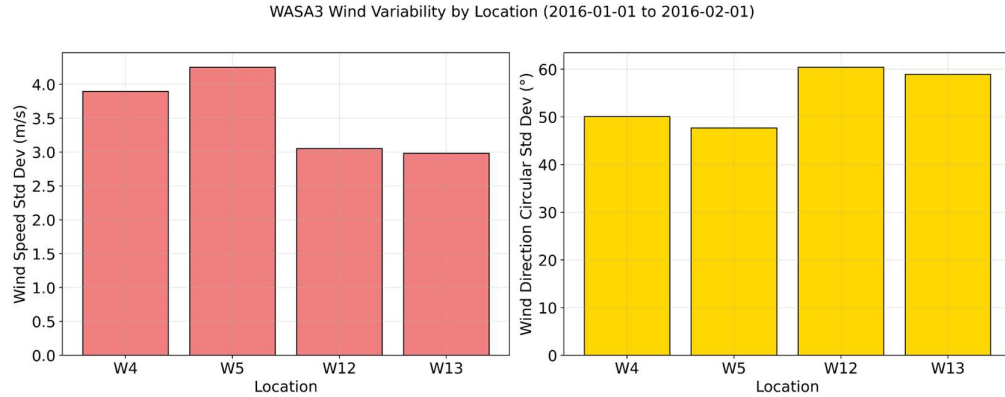


Figure 23) WASA3 winds variability at grid cells east and west of the ADCP deployments for January 2016.

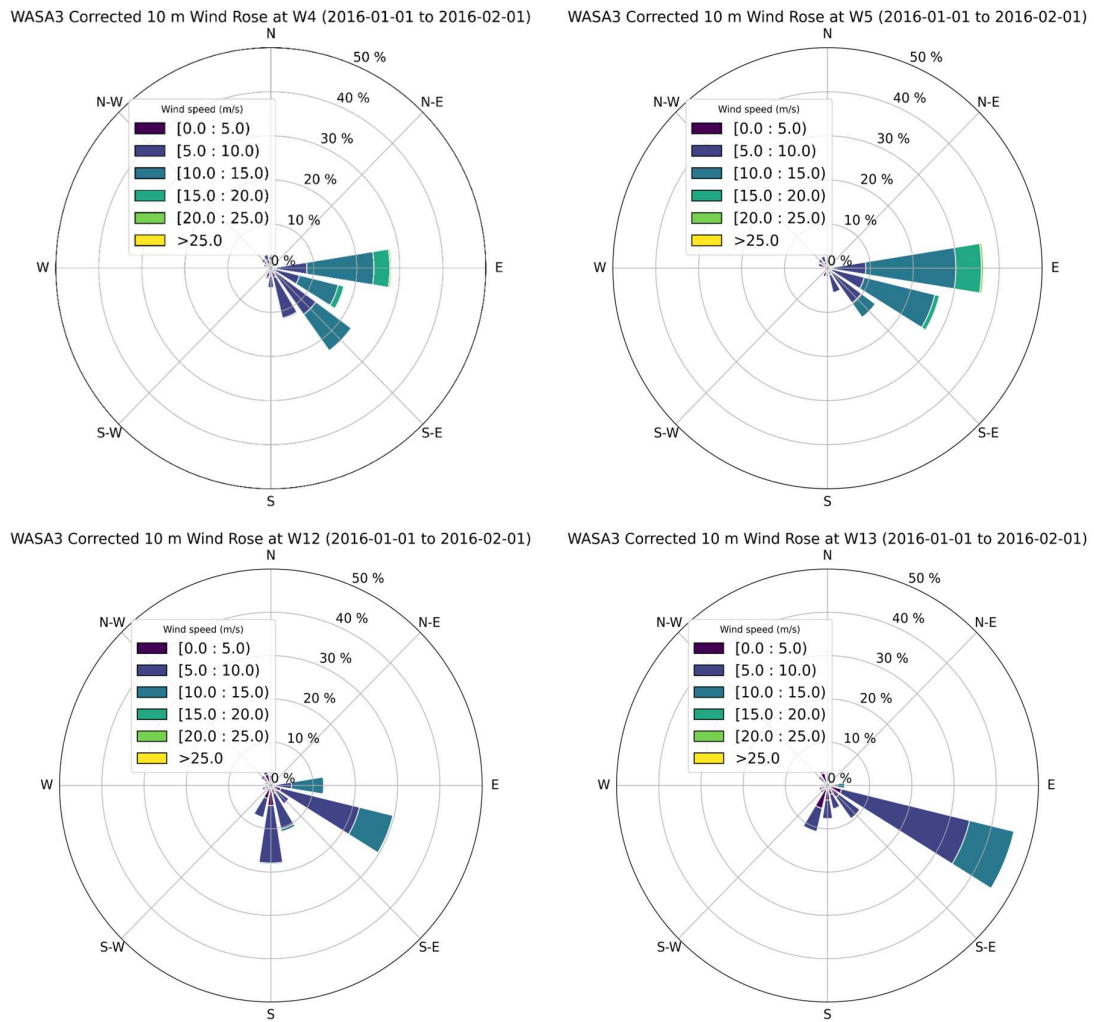


Figure 24) Wind roses for January 2016 at the WASA3 grid cells located east and west of the ADCP deployments.

4.2.2.3 Comparison: ERA5 vs WASA3

Both datasets yielded similar mean wind speeds, broadly consistent with historical observations of False Bay (Atkins, 1970b; Le Roux, 1975; Gründlingh, Hunter and Potgieter, 1989; Bonnardot, Planchon and Cautenet, 2005). However, their agreement in temporal variability was alarmingly poor ($r=0.06$), and the timing of wind events showed no clear phase relationship (Fig. 25). Wind directions also diverged: ERA5 exhibited a predominantly southeasterly baseline, whereas WASA3 showed more frequent easterly flow. The higher resolution WASA3 dataset revealed distinct diurnal directional shifts, typically easterly during the night or early morning and southeasterly during the day, consistent with observations by Bannardot et al. (2005). In contrast, ERA5 captured broader 3–5 day synoptic cycles characteristic of summer southeasterly wind events but did not capture finer temporal variability. Peaks in wind speed typically correspond to southeasterlies in both datasets.

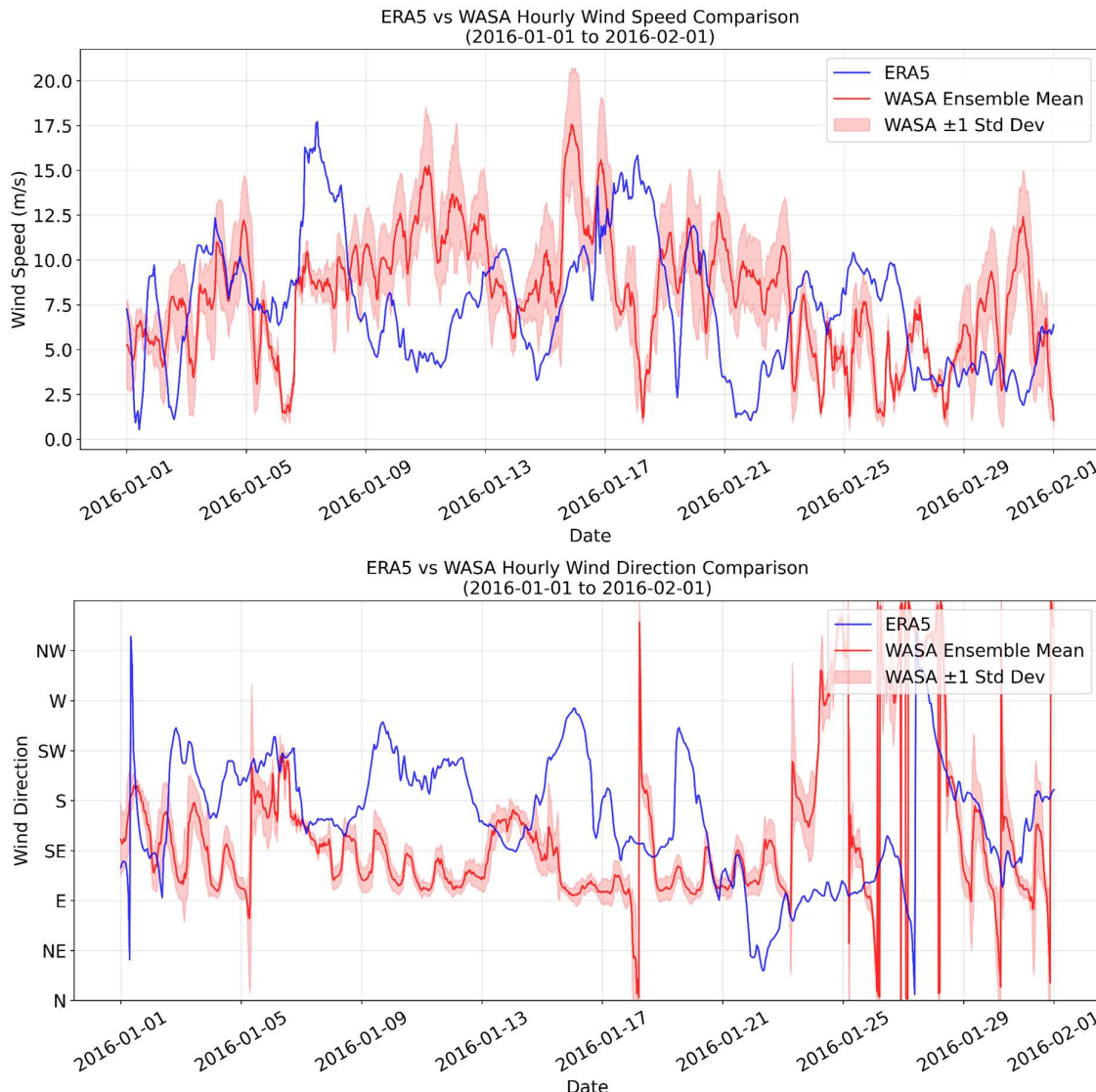


Figure 25) Comparison of mean hourly wind speed (top) and wind direction (bottom) between WASA3 (red line) and ERA5 (blue line). The shaded area indicates one standard derivation around the WASA3 mean.

4.2.3 ADCP Diagnostics

The Level 2 dataset from the Gordon's Bay deployment comprised 69 120 measurements collected between 01 January and 01 February 2016. Of these, 71.7 % — 49 539 measurements — were valid. The majority of invalid points corresponded to bins located above the sea surface (Fig. 26), a result of the ADCP's 30 one-metre bin configuration during deployment. Error velocity statistics indicated that the instrument performed well, with a mean error velocity near zero ($-0.0015 \pm 0.0211 \text{ m s}^{-1}$).

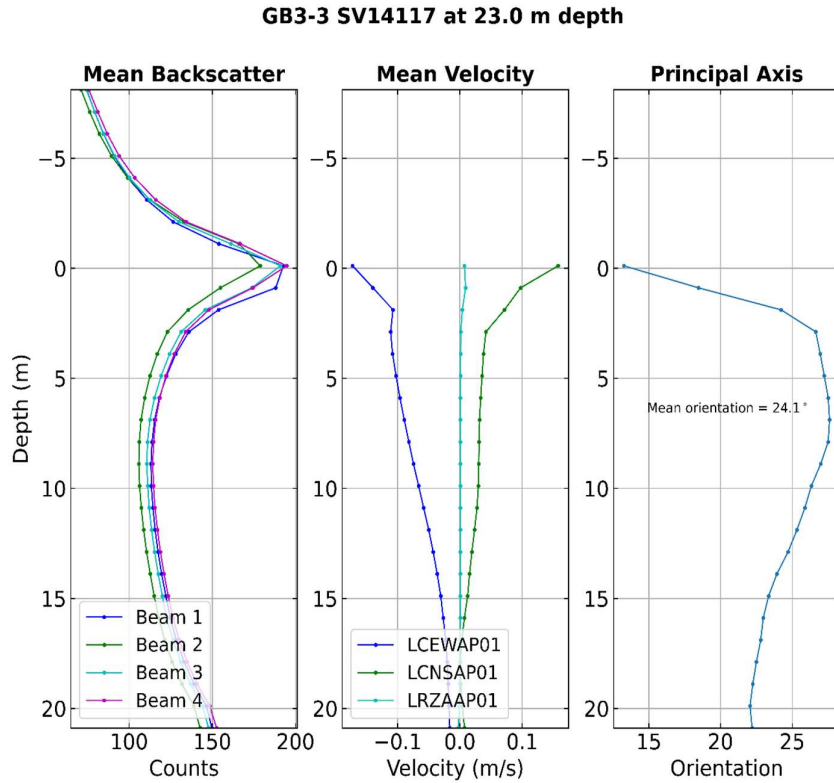


Figure 26) Diagnostic plot for L2 Gordon's Bay D3 data.

Table 3) Echo Intensity Statistics

Beam Number	Mean Backscatter Counts	Standard Deviation
1 (zonal)	123.83	35.80
2 (meridional)	117.00	30.13
3 (vertical)	121.90	31.51
4 (error)	125.22	31.96

The four acoustic beams exhibited similar mean backscatter counts and variability, confirming consistent performance across zonal, meridional, vertical and error velocity channels (Table 3). Horizontal velocity components contained 24.5 % probably good data (Flag 3) and 26.3 % bad data (Flag 4) (Fig. 27). Flags 3 and 4 were primarily triggered by negative pressure values and increasing backscatter intensity with depth. Overall, the dataset is considered reliable.

GB3-3 SV14117 at 23.0 m depth: L2 QC

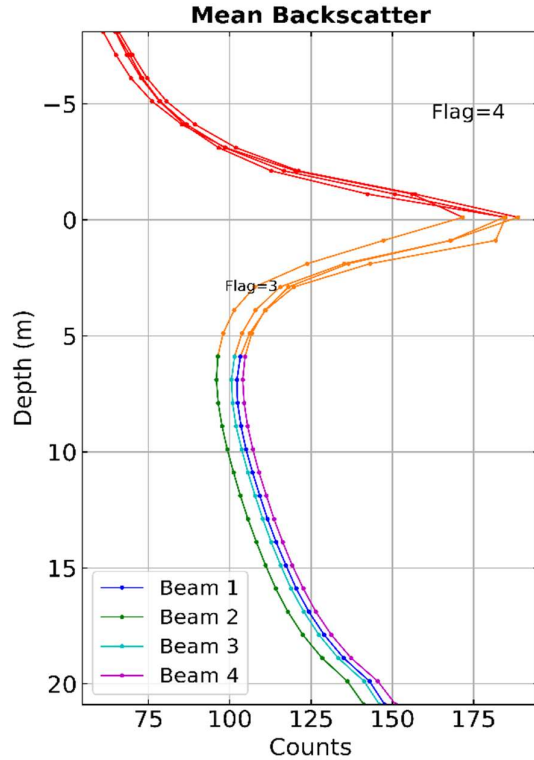


Figure 27) Mean backscatter associated with each beam. Flags 3 and 4 label suspicious and bad data respectively.

4.2.4 Waves

4.2.4.1 Wave Height and Period

Wave measurements from January 2016 (186 burst samples over 31 days) revealed moderate wave conditions typical of the northeasterly portion of False Bay during summer. The mean significant wave height (H_s) was $1.41 \pm 0.37\text{ m}$, ranging from 0.58 to 2.37 m (Fig. 28). Maximum wave heights (H_{\max}) averaged 2.17 m, with a recorded maximum of 3.70 m. These values are consistent with historical observations in the bay (Joubert, 2008; Veitch *et al.*, 2019). Only eight events exceeded $H_s = 2.0\text{ m}$, and none exceeded 3.0 m, confirming a generally moderate wave regime during this period.

Peak wave periods (T_p) were variable, with a mean of $10.7 \pm 3.3\text{ s}$ ranging between 2.9 – 22.8 s. While most values fall within the expected 8–14 s range for the region (van Verwolde, 2004), anomalously long periods ($> 16\text{ s}$) were occasionally detected. Although long-period swells can occur during the passage of cold fronts during winter (van Verwolde, 2004), these instances occurred under low-energy conditions, suggesting they are likely artifacts and of the proprietary WavesMon processing algorithm (Fig. 28). Consequently, these long-period values should be interpreted with caution, as they are most likely overestimations by WavesMon.

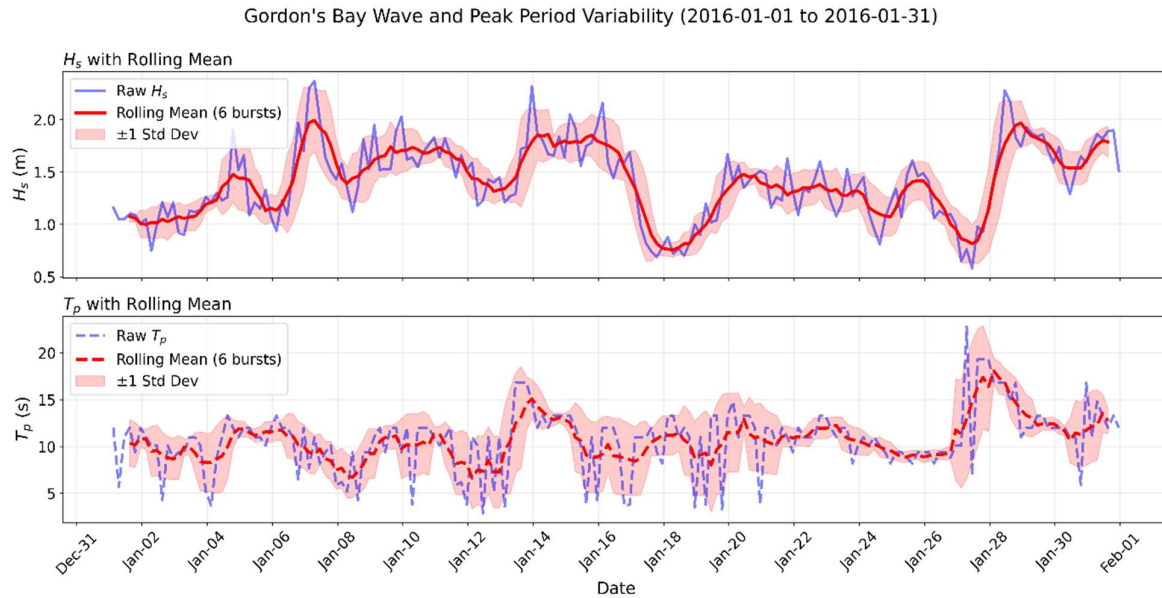


Figure 28 Analysis of the variability of significant wave height and peak period measured by the Gordon's Bay ADCP during January 2016. The top panel shows the raw significant wave height (H_s , blue line) and its rolling mean (red line). The bottom panel shows the raw peak period (T_p , dashed blue line) and its rolling mean (dashed red line). Red shading indicates one standard deviation. Each rolling mean is calculated over a one-day window, with individual burst every 4 hours.

4.2.4.2 Sea-Swell Partitioning

The wave field demonstrated mixed sea-swell conditions, with sea-dominated conditions occurring 53.8 % of the time and swell-dominated conditions 43.5 % of the time (Fig 29). WavesMon partitions the wave spectrum based on a cutoff frequency, which by default is 0.125 Hz. Wind-sea components ($H_{s,sea} = 0.99 \pm 0.32 \text{ m}$, $T_{p,sea} = 5.7 \pm 1.5 \text{ s}$) and swell components ($H_{s,swell} = 0.97 \pm 0.34 \text{ m}$, $T_{p,swell} = 11.7 \pm 2.4 \text{ s}$) contributed nearly equally to total wave energy.

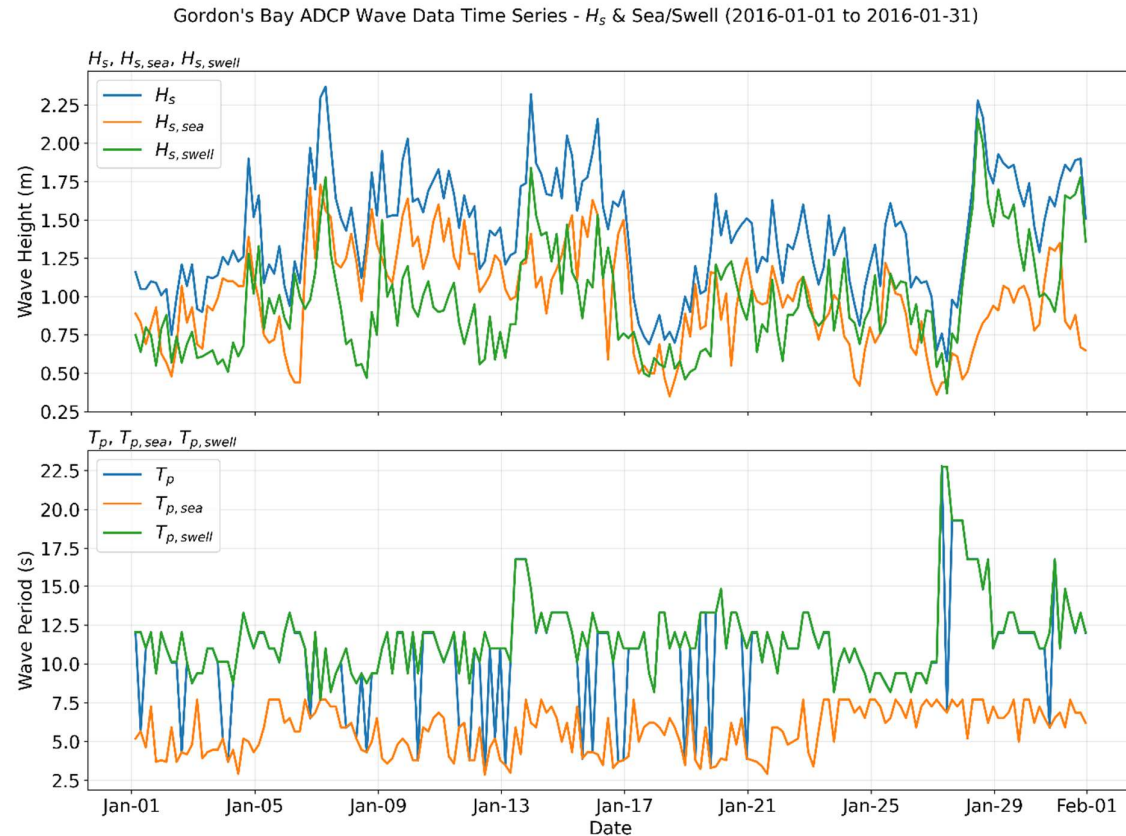


Figure 29) Time series of frequency-domain wave parameters from the Gordon's Bay ADCP during January 2016. The top panel shows the total significant wave height (H_s) and its decomposition sea ($H_{s,sea}$) and swell ($H_{s,swell}$) components. The bottom panel shows the corresponding peak periods (T_p , $T_{p,sea}$, and $T_{p,swell}$).

4.2.4.3 Wave Direction

The mean wave direction was from the southwest, consistent with the Cape Point Wave Record (Veitch et al., 2019). Swell periods were notable longer and exhibited more consistent directionality ($D_{p,swell} = 221 \pm 8^\circ$) compared to wind-sea ($D_{p,sea} = 205 \pm 37^\circ$), indicating a combination of well-organized distant swells from the southwest and locally generated wind waves (Fig. 30).

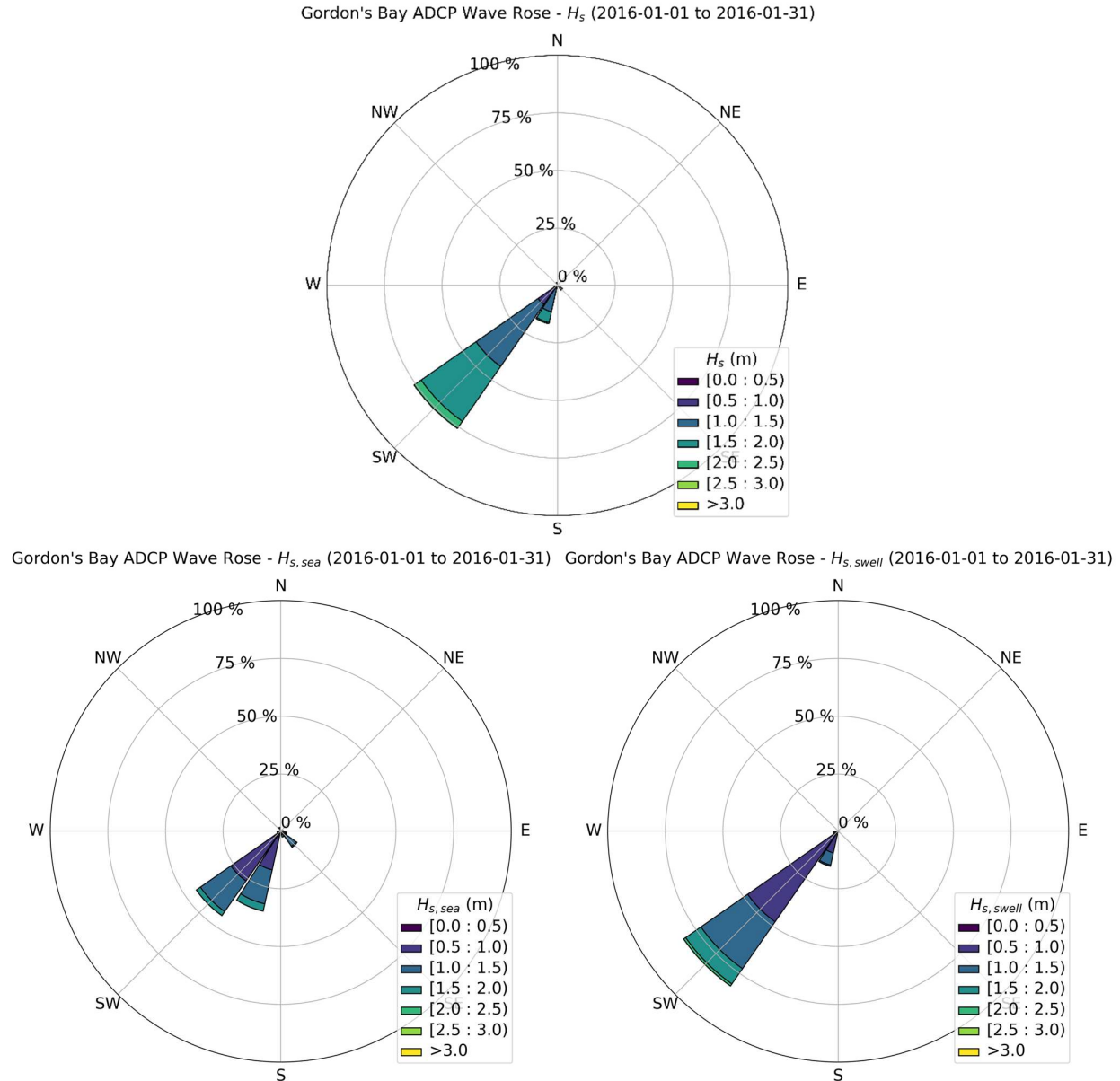


Figure 30) Directional distribution of significant wave height (H_s) measured by the Gordon's Bay ADCP during January 2016. The top panel shows the total wave field, while the lower panels show the respective contributions from the sea (left) and swell (right) components.

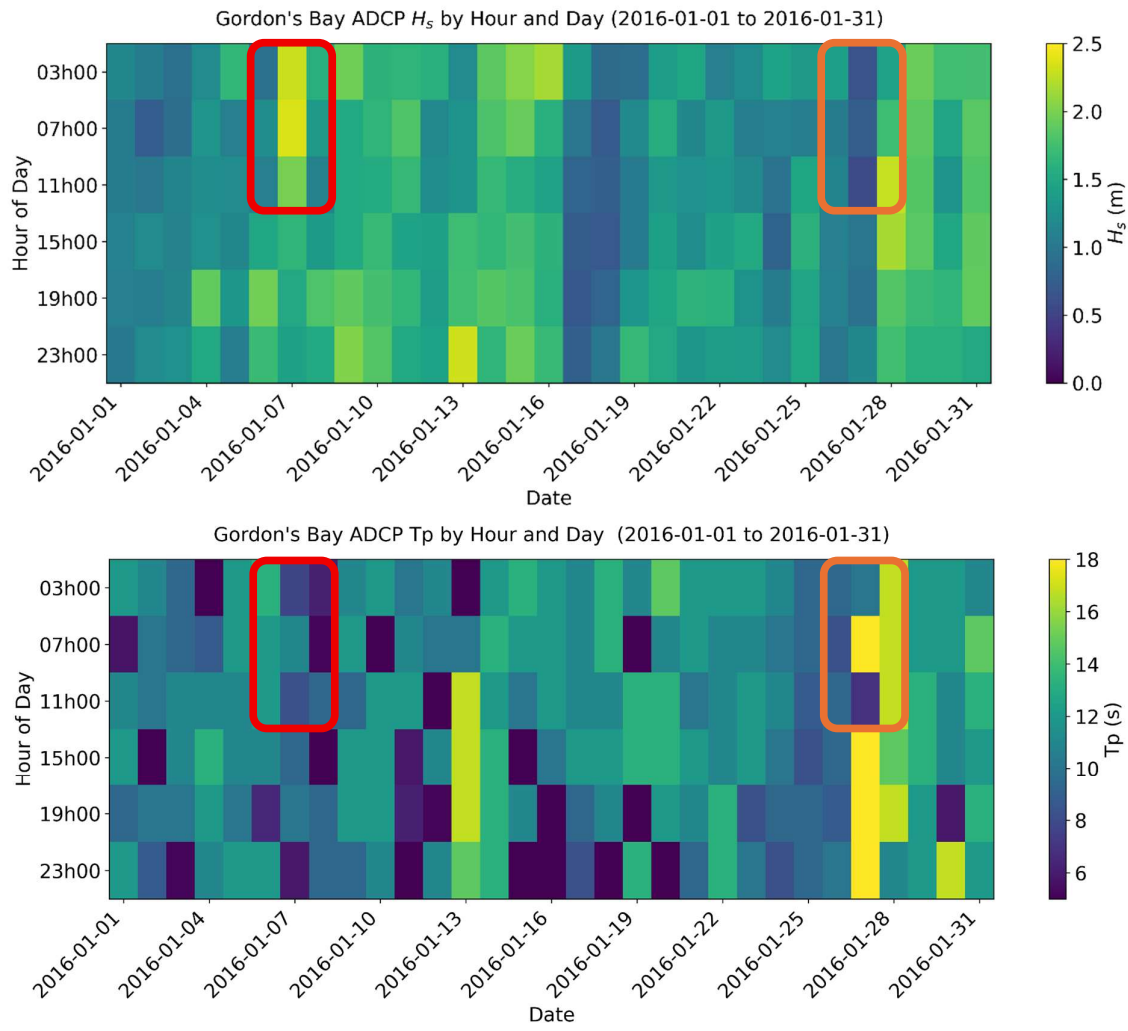


Figure 31) Hovmöller diagrams recorded by the Gordon's Bay ADCP during January 2016. The top panel shows significant wave height (H_s), and the bottom panel shows the peak wave period (T_p). Each day consists of six 4-hour bursts.

These 4-hourly wave data complement the high-frequency current and wind observations, providing insight into the local variability and vertical structure of currents. On 07 January 2016 (red box, Fig. 31), the significant wave height peaks around 2.5 m at approximately 07h00 UTC, with a relatively low peak period, indicative of a wave field dominated by local winds. In contrast, on 27 January (orange box), wave heights remain low, but the WavesMon algorithm occasionally produces sudden jumps from low to high peak periods. This reflects the algorithm's difficulty in accurately resolving calm, swell-dominated conditions, illustrating a limitation of the proprietary processing software even when it remains a useful tool for distinguishing wind- and swell-dominated events.

4.2.4.4 Wave Energy Spectrum During Wind and Swell Dominated Conditions

Currently, there is no open-source method to directly extract or reproduce wave spectra from raw Teledyne RDI Workhorse ADCP data. Teledyne's WavesMon remains the only tool for visualising these spectra, and it has not been updated since 2011. This limitation affects reproducibility, aesthetics and integration into operational oceanography systems. Despite these shortcomings, the visualisations still provide valuable information, showing how the total wave energy is distributed across frequencies, offering a qualitative sense of the wave field (Fig. 32).

On 7 January 2016, the spectral peak lies around 0.9 Hz, corresponding to a wave period of approximately 9 seconds, indicative of a wave field dominated by locally generated wind waves. On the 27 January, the peak is around 0.14 Hz, corresponding to 14 seconds, suggesting incoming swell. However, uncertainty introduced by low wave heights and jumps in the calculated period is not captured in this visualisation, highlighting the importance of cross-checking wave parameters before drawing conclusions about the wave field.

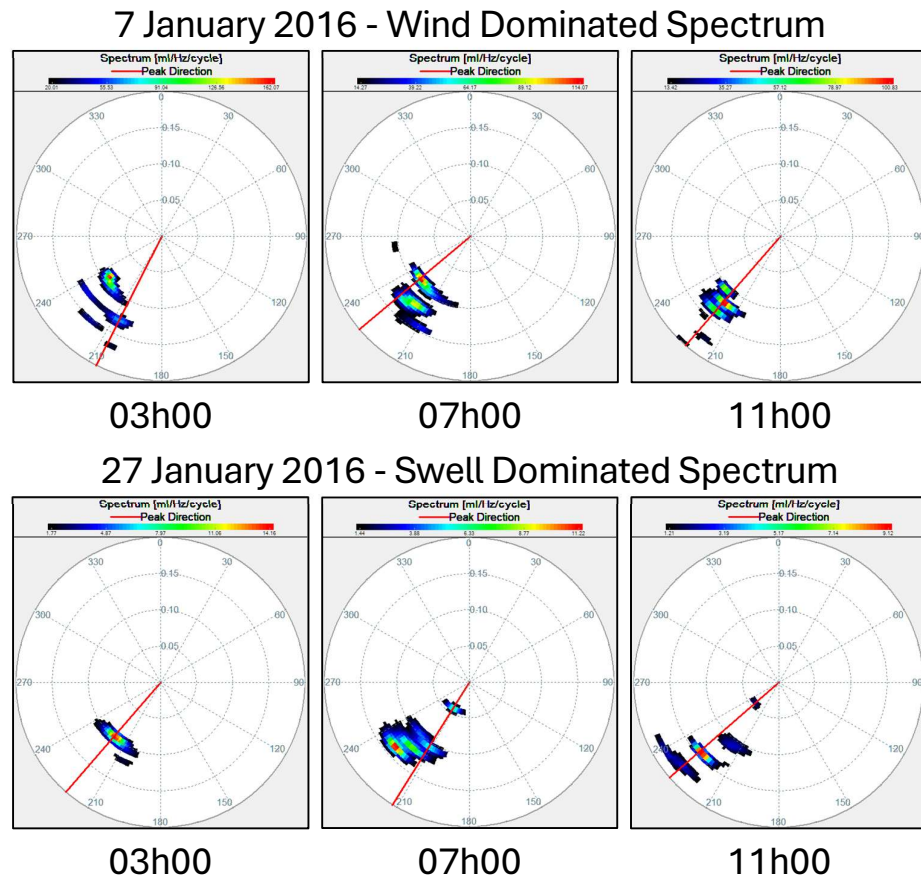


Figure 32) Wave energy spectra from the Gordon's Bay ADCP illustrating two conditions: a wind dominated wave field (7 January 2016), and a swell dominated wave field (27 January 2016). The red line indicates the direction of incident waves, measured in degrees clockwise from north. The radial axis represents frequency (Hz).

4.2.5 Conclusion

The contrasting behaviour of ERA5 and WASA3 highlights the challenge of accurately representing nearshore wind variability in complex coastal terrain. On 7 January 2016, ERA5 captured strong south-southeasterly winds and the ADCP recorded large waves with short peak periods, consistent with a locally forced wind-sea (Fig. 32). In contrast, WASA3 underestimated this event. The ADCP also detected a slight increase in current velocity throughout the water column, likely indicating a wind-driven response. On 27 January, both datasets showed weak winds, while the ADCP recorded rising significant wave heights and anomalously long periods, likely an artefact of the proprietary processing algorithm. This coincided with weak, depth varying currents, confirming the presence of a calm sea state.

Finally, there are several periods between 9 and 25 January when WASA3 winds were stronger than those from ERA5, yet the ADCP recorded high significant wave heights and long peak periods. This suggests a combination of a locally forced wind-sea and incoming swell. Direct access to wave spectra would be invaluable here, as identifying the frequency associated with the peak energy would clarify which mechanism – wind or swell – dominates at a given time. These intervals of higher WASA3 winds coincide with strong current reversals detected by the ADCP, implying that these reversals were driven by local wind forcing modified by orographic events, which ERA5 fails to capture.

This study directly addressed the critical lack of oceanographic time-series data in False Bay, where much of the existing data has remained underutilised due to reliance on costly and outdated proprietary software. To address this, we adapted an existing open-source workflow capable of recovering and processing archival Teledyne RDI Workhorse ADCP data. We demonstrated the utility of this approach through a case study investigating local oceanographic processes, thereby contributing valuable time-series data to an observation-scarce region. In doing so, we also identified where open-source capabilities still need to be developed — such as for extracting and visualising wave spectra – and where existing open-source tools require improvement, including workarounds for frequency-related processing bugs.

The data recovered in this study were processed with the next step in the operational oceanographic system in mind: integration into ocean prediction frameworks. These datasets can support ongoing operational oceanography efforts in South Africa and provide insight into the local oceanographic processes that must be considered in future coastal management and planning. More broadly, the successful processing of raw data from a ‘legacy’ instrument demonstrates that such instruments, when still operational, can be redeployed to generate high quality datasets and extend the lifespan of existing oceanographic infrastructure — an important consideration in a field increasingly constrained by limited funding and uncertainty about future research opportunities.

Collectively, this work demonstrates the value of revisiting and revitalising historical oceanographic datasets through open-source tools. By bridging the gap between legacy instrumentation and modern data processing, it offers both a methodological framework and new insights into False Bay’s dynamic coastal system. In doing so, it lays a foundation for more transparent, reproducible, and sustainable ocean observation practises in South Africa and beyond.

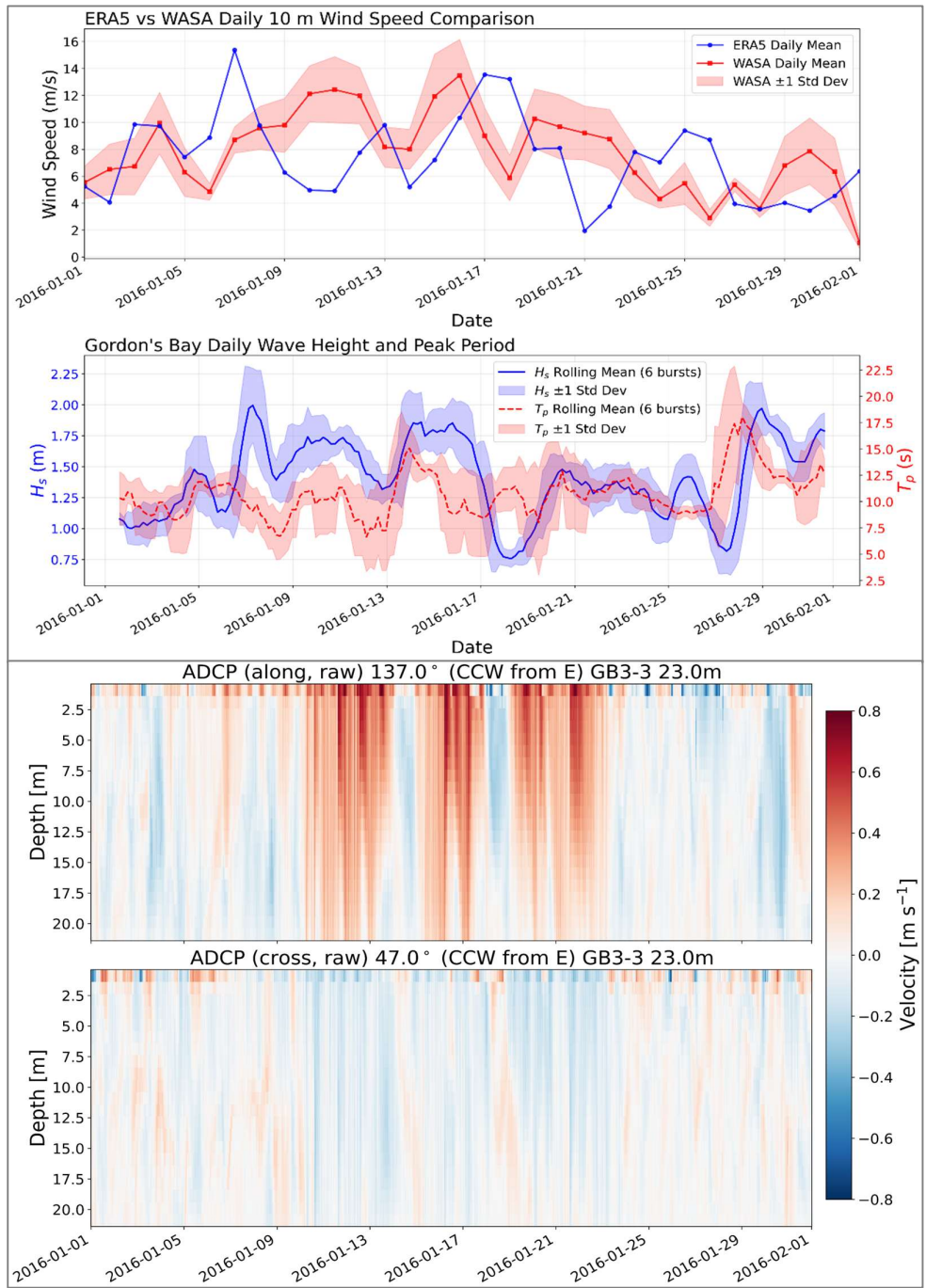


Figure 32) Summary of the wind, wave and current fields at the Gordon's Bay ADCP during January 2016. **Top panel:** Daily mean 10 m wind speed from ERA5 (blue line) and the WASA3 ensemble (red line), with one standard deviation of WASA3 indicated by red shading (top plot). Daily mean significant wave height (H_s , blue line) and corresponding peak period (T_p , red line) are shown in the bottom plot of the top panel, with one standard deviation indicated by shading (bottom plot). **Bottom panel:** Alongshore and cross-shore velocity profiles from unfiltered L2 ADCP data at Gordon's Bay D3.

5 BIBLIOGRAPHY

- Amol Prakash (2025) “pyadps.” Available at: <https://pyadps.readthedocs.io/en/latest/index.html#>.
- Andrew Simms *et al.* (2025) “MHKit-Software/MHKit-MATLAB: MHKit-MATLAB v0.6.0 Release.” Zenodo. Available at: <https://doi.org/10.5281/ZENODO.14885270>.
- AODN (2019) “IMOS Toolbox.” Australia: Australian Ocean Data Network. Available at: <https://github.com/aodn/imos-toolbox>.
- Atkins, G.R. (1970a) “Thermal Structure and Salinity of False Bay,” *Transactions of the Royal Society of South Africa*, 39(2), pp. 117–128. Available at: <https://doi.org/10.1080/00359197009519107>.
- Atkins, G.R. (1970b) “Winds and Current Patterns in False Bay,” *Transactions of the Royal Society of South Africa*, 39(2), pp. 139–148. Available at: <https://doi.org/10.1080/00359197009519109>.
- Bang, N. and Andrews, W. (1974) “Direct current measurements of a shelf-edge frontal jet in the southern Benguela system,” *Journal of Marine Research*, 32(3). Available at: https://elischolar.library.yale.edu/journal_of_marine_research/1299.
- Bart Vermeulen (2021) “adcptools.” Wageningen. Available at: <https://github.com/bartverm/adcptools?tab=readme-ov-file#readme>.
- Bonnardot, V., Planchon, O. and Cautenet, S. (2005) “Sea breeze development under an offshore synoptic wind in the South-Western Cape and implications for the Stellenbosch wine-producing area,” *Theoretical and Applied Climatology*, 81(3), pp. 203–218. Available at: <https://doi.org/10.1007/s00704-004-0087-y>.
- Boyd, A. *et al.* (2014) “Determination of the Inshore wave climate along the South African coast - Phase 1 for Coastal Hazard and Vulnerability Assessment.”
- Brown, A. *et al.* (2012) “Unified Modeling and Prediction of Weather and Climate: A 25-Year Journey.” Available at: <https://doi.org/10.1175/BAMS-D-12-00018.1>.
- Climate Systems Analysis Group (2016) *Climate Change Projections for the City of Cape Town: An Update Based on the Most Recent Science*. Cape Town: Climate Systems Analysis Group, University of Cape Town. Available at: http://www.csag.uct.ac.za/~cjackson/CSAG_CCT%20report.pdf.
- Coleman, F. (2019) *The Development and Validation of a Hydrodynamic Model of False Bay*. Master of Engineering. Stellenbosch University. Available at: <https://core.ac.uk/outputs/196259848/?source=2> (Accessed: July 29, 2025).
- Colenbrander, D. (2017) “Maintenance Management Plan: Dunes and Beaches.” City of Cape Town.
- CSIR (1982) *Status Report on Pollution in False Bay*. CSIR Report C/SEA 8241. Stellenbosch, South Africa: CSIR.
- Cullen, M.J.P. (1993) *The unified forecast/climate model*. Bracknell: Meteorological Office, pp. 233–260.
- Daniels, T. *et al.* (2022) “On the importance of wind generated waves in embayments with complex orographic features – A South African case study,” *Applied Ocean Research*, 128, p. 103355. Available at: <https://doi.org/10.1016/j.apor.2022.103355>.
- Davidson, F. *et al.* (2019) “Synergies in Operational Oceanography: The Intrinsic Need for Sustained Ocean Observations,” *Frontiers in Marine Science*, 6. Available at: <https://doi.org/10.3389/fmars.2019.00450>.

Dufois, F. and Rouault, M. (2012) "Sea surface temperature in False Bay (South Africa): Towards a better understanding of its seasonal and inter-annual variability," *Continental Shelf Research*, 43, pp. 24–35. Available at: <https://doi.org/10.1016/j.csr.2012.04.009>.

Flemming, B.W. (2024) "Sedimentology of False Bay (Western Cape, South Africa): geological background information for the integrated environmental management of a physically confined coastal compartment," *Journal of Coastal Conservation*, 28(6), pp. 1–23. Available at: <https://doi.org/10.1007/s11852-024-01080-z>.

Fourie, J.P. et al. (2015) "The influence of wave action on coastal erosion along Monwabisi Beach, Cape Town," *South African Journal of Geomatics*, 4(2), pp. 96–109. Available at: <https://doi.org/10.4314/sajg.v4i2.3>.

Gill, A.E. (1977) "Coastally trapped waves in the atmosphere," *Quarterly Journal of the Royal Meteorological Society*, 103, pp. 431–440.

Gründlingh, M.L. (1992) "Quasi-synoptic survey of the thermohaline properties of False Bay," *South African Journal of Science*, 88, pp. 325–334.

Gründlingh, M.L., Hunter, I.T. and Potgieter, E. (1989) "Bottom currents at the entrance to False Bay, South Africa," *Continental Shelf Research*, 9(12), pp. 1029–1048. Available at: [https://doi.org/10.1016/0278-4343\(89\)90056-3](https://doi.org/10.1016/0278-4343(89)90056-3).

Gunnar Voet (2015) "mADCP" La Jolla: Scripps Institution of Oceanography (Multiscale Ocean Dynamics). Available at: <https://github.com/modscripps/mADCP/tree/master>.

Hahmann, A.N. et al. (2021) "The WASA3 Numerical Wind Atlas – Methods and validation," 29 October. Available at: https://www.wasaproject.info/temp/WASA_3_Virtual_Wind_Seminar/Andrea%20N%20Hahmann%2C%20Rogier%20Floors%20DTU.pdf (Accessed: September 25, 2025).

Hana Hourston et al. (2023) "pycurrents_ADCP_processing." Canada: IOS OSD Data Product Team. Available at: https://github.com/IOS-OSD-DPG/pycurrents_ADCP_processing?tab=readme-ov-file.

Hersbach, H. et al. (2020) "The ERA5 global reanalysis," *Quarterly Journal of the Royal Meteorological Society*, 146(730), pp. 1999–2049. Available at: <https://doi.org/10.1002/qj.3803>.

Holthuijsen, L. (2007) "Waves in Oceanic and Coastal Waters," *Waves in Oceanic and Coastal Waters*, by Leo H. Holthuijsen, pp. 404. Cambridge University Press, January 2007. ISBN-10: . ISBN-13: [Preprint]. Available at: <https://doi.org/10.2277/0521860288>.

Isaac, W.E. (1937) "South African Coastal Waters in Relation to Ocean Currents," *Geographical Review*, 27(4), pp. 651–664. Available at: <https://doi.org/10.2307/209863>.

Jacobson, M. (2014) *The influence of a spatially varying wind field on the circulation and thermal structure of False Bay during summer: a numerical modelling study*. Honours Thesis. University of Cape Town.

Joubert, J.R. (2008) *An investigation of the wave energy resource on the South African coast, focusing on the spatial distribution of the south west coast*. Stellenbosch: University of Stellenbosch.

Jury, M.R. (1984) *Wind shear and differential upwelling along the SW tip of Africa*. Ph.D. thesis. University of Cape Town.

Jury, M.R. (1991) "The weather of False Bay," *Transactions of the Royal Society of South Africa*, 47, pp. 401–418.

- Jury, M.R., Kamstra, F. and Taunton-Clark, J. (1985) "Diurnal wind cycles and upwelling off the northern portion of the Cape Peninsula in summer," *South African Journal of Marine Science*, 3(1), pp. 1–10. Available at: <https://doi.org/10.2989/025776185784461216>.
- Kelley, D. and Richards, C. (2025) "oce: Analysis of Oceanographic Data." Available at: <https://dankelley.github.io/oce/>.
- Largier, J.L. et al. (1992) "The western Agulhas Bank: circulation, stratification and ecology," *South African Journal of Marine Science*, 12(1), pp. 319–339. Available at: <https://doi.org/10.2989/02577619209504709>.
- Le Roux, J.J. (1975) *Climate of South Africa, Part 1: Surface winds*. Report WB 38. South Africa: South African Weather Bureau, Dept. Transport, p. 79.
- Lennard, C. et al. (2021) "Wind Time Series for WASA3 Domain, South Africa." University of Cape Town (UCT) and DTU Wind Energy.
- Lucas Merckelbach (2017) "adcpreader." Available at: <https://github.com/smercke/adcpreader>.
- MacHutchon, K.R. (2006) *The Characterisation of South African Sea Storms*. Ph.D. thesis. Stellenbosch University.
- Mallory, J.K. (1970) "The Bathymetry and Microrelief of False Bay," *Transactions of the Royal Society of South Africa*, 39(2), pp. 109–112. Available at: <https://doi.org/10.1080/00359197009519105>.
- Marinna Martini (2020) "ADCPy." United States Geological Survey. Available at: <https://github.com/mmartini-usgs/ADCPy>.
- Massel, S.R. (2017) *Ocean surface waves: their physics and prediction*. 3rd ed. World scientific.
- Nicholson, S.A. (2011) *The circulation and thermal structure of False Bay: a process-oriented numerical modelling and observational study*. MSc thesis. University of Cape Town.
- Pfaff, M.C. et al. (2019) "A synthesis of three decades of socio-ecological change in False Bay, South Africa: setting the scene for multidisciplinary research and management," *Elementa: Science of the Anthropocene*. Edited by J.W. Deming, 7, p. 32. Available at: <https://doi.org/10.1525/elementa.367>.
- Ramos, M.S. et al. (2021) "Relationships between large-scale climate modes and the South Atlantic Ocean wave climate," *Progress in Oceanography*, 197, p. 102660. Available at: <https://doi.org/10.1016/j.pocean.2021.102660>.
- Robinson, A.R. and Lermusiaux, P.F.J. (2001) "Data Assimilation In Models," in J.H. Steele (ed.) *Encyclopedia of Ocean Sciences*. Oxford: Academic Press, pp. 623–634. Available at: <https://doi.org/10.1006/rwos.2001.0404>.
- Salonen, N.M. (2019) *Towards Rogue Wave Characterization in False Bay, South Africa*. Available at: <https://hdl.handle.net/11427/31709> (Accessed: August 4, 2025).
- Shillington, F.A. and Wyndham Harris, T.F. (1978) "Surface waves near Cape Town and their associated atmospheric pressure distributions over the South Atlantic," *Deutsche Hydrographische Zeitschrift*, 31(3), pp. 67–82. Available at: <https://doi.org/10.1007/BF02227005>.
- Shipley, A.M. (1964) "Some aspects of wave refraction in False Bay," *South African Journal of Science*, 60(6), pp. 115–120. Available at: https://doi.org/10.10520/AJA00382353_1513.
- Singleton, A.T. and Reason, C.J.C. (2007) "Variability in the characteristics of cut-off low pressure systems over subtropical southern Africa," *International Journal of Climatology*, 27(3), pp. 295–310. Available at: <https://doi.org/10.1002/joc.1399>.

Taljaard, A.J. et al. (1969) "Climate of the Upper Air: Southern Hemisphere: Volume 1: Temperatures, Dew Points, and Heights at Selected Pressure Levels." Available at: <https://n2t.org/ark:/85065/d7h131fh>.

Taljaard, S., van Ballegooyen, R. and Morant, P. (2000) *False Bay Water Quality Review — Volume 2: Specialist Assessments and Inventories of Available Literature and Data*. CSIR Report ENV-S-C 2000-086/2. Stellenbosch, South Africa: Council for Scientific and Industrial Research.

Teledyne RD Instruments (2018) "Velocity Tools - Data Processing Software."

Thomson, R.E. and Emery, W.J. (2024) "Digital Filters," in *Data Analysis Methods in Physical Oceanography*. Elsevier, pp. 671–710. Available at: <https://doi.org/10.1016/B978-0-323-91723-0.00001-5>.

Turpie, J.K. et al. (2017) "Mapping and valuation of South Africa's ecosystem services: A local perspective," *Ecosystem Services*, 27, pp. 179–192. Available at: <https://doi.org/10.1016/j.ecoser.2017.07.008>.

Van Foreest, D. and Jury, M.R. (1985) "A numerical model of the wind-driven circulation in False Bay," *South African Journal of Science*, 81, pp. 312–317.

Veitch, J. et al. (2019) "The Cape Point wave record, extreme events and the role of large-scale modes of climate variability," *Journal of Marine Systems*, 198, p. 103185. Available at: <https://doi.org/10.1016/j.jmarsys.2019.103185>.

van Verwolde, E. (2004) *Characteristics of extreme wave events and the correlation between atmospheric conditions along the South African coast*. Master's Thesis. University of Cape Town.

de Vos, M. (2022) *Modelling waves and near-shore circulation around the Cape Peninsula: towards enhanced predictions for South African coastal activities*. Doctor of Philosophy. University of Cape Town. Available at: <http://hdl.handle.net/11427/37123> (Accessed: July 29, 2025).

Wainman, C.K., Polito, A. and Nelson, G. (1987) "Winds and subsurface currents in the False Bay region, South Africa," *South African Journal of Marine Science*, 5(1), pp. 337–346. Available at: <https://doi.org/10.2989/025776187784522423>.

World Meteorological Organization (WMO) (2024) *Guide to Instruments and Methods of Observation (WMO-No. 8), Volume I – Measurement of Meteorological Variables*. 2024th ed. World Meteorological Organization (WMO). Available at: <https://doi.org/10.59327/WMO/CIMO/1>.

6 APPENDIX

6.1 ADCP PROCESSING ENVIRONMENT SETUP

Pre-requisites

- OS: Ubuntu / Windows Subsystem for Linux 2
 - Python version: **3.7** (installation instructions included)
 - Tools: git, pip, conda, and mercurial
-

Step-by-step Installation

1. Install Miniconda (skip if already installed)

- a) Open a terminal in Ubuntu.
- b) Copy the first command from the grey box below into the terminal.
- c) Press Enter and let it finish.
- d) Repeat steps b) and c).

```
wget https://repo.anaconda.com/miniconda/Miniconda3-latest-Linux-x86_64.sh  
bash Miniconda3-latest-Linux-x86_64.sh  
source ~/.bashrc
```

2. Create a working directory and Python 3.7 environment

```
mkdir ~/adcp  
cd ~/adcp  
  
conda create -n adcp37 python=3.7  
conda activate adcp37
```

3. Configure Conda and install base dependencies

```
conda config --add channels conda-forge  
conda config --set channel_priority strict  
  
conda install numpy scipy pip pandas netCDF4 xarray gsw matplotlib=3.5 shapely  
cython  
pip install ruamel.yaml
```

4. Clone and install ttide_py in editable mode

```
git clone https://github.com/moflaher/ttide_py.git  
cd ttide_py
```

```
pip install -e .
cd ..
```

5. Clone and install pycurrents in editable mode

```
sudo apt install mercurial # needed for `hg clone`

hg clone http://currents.soest.hawaii.edu/hg/pycurrents
cd pycurrents
pip install -e .
cd ..
```

6. Clone and install pycurrents_ADCP_processing in editable mode

```
git clone https://github.com/IOS-OSD-DPG/pycurrents_ADCP_processing.git
cd pycurrents_ADCP_processing
pip install -e .
cd ..
```

7. Test the environment

Launch Python and verify paths:

```
python
import pycurrents
print(pycurrents.__file__)

import pycurrents_ADCP_processing
print(pycurrents_ADCP_processing.__file__)

import ttide
print(ttide.__file__)
```

You should see paths like:

```
/home/ethan/adcp/pycurrents/pycurrents/__init__.py
/home/ethan/adcp/pycurrents_ADCP_processing/pycurrents_ADCP_processing/__init__.py
/home/ethan/adcp/ttide_py/ttide/__init__.py
```

If you see paths like this:

```
/home/ethan/miniconda3/envs/adcp37/lib/python3.7/site-
packages/pycurrents_ADCP_processing
```

Something has gone wrong.

Optional: Cleanup from Old Installations

If you're reinstalling or correcting a broken setup, you can clean old installs:

```
pip uninstall pycurrents pycurrents_ADCP_processing ttide
rm -rf pycurrents/*.egg-info pycurrents_ADCP_processing/*.egg-info ttide_py/*.egg-
info
```

Also inspect and clean:

```
rm -rf ~/miniconda3/envs/adcp37/lib/python3.7/site-packages/*pycurrents*
rm -rf ~/miniconda3/envs/adcp37/lib/python3.7/site-packages/*ttide*
```

6.2 LAUNCHING PYCURRENTS IN JUPYTERLAB.

Usage:

1. Launch an Ubuntu terminal and set up the working directory in Jupyter Lab

In Ubuntu:

```
cd ~/adcp
conda activate adcp37
jupyter lab --port 8888 --no-browser
```

In Jupyter Lab, launch a terminal and activate the venv.

```
conda activate adcp37
```

2. Create a working copy of create_nc.py in
~/adcp/pycurrents_ADCP_processing/pycurrents_ADCP_processing

For GB1 I duplicated the original create_nc.py file and named it create_nc_GB1.py

3. Open the file and define the raw ADCP file and associated metadata file

```
raw data:
"\\"wsl.localhost\Ubuntu\home\ethan\adcp\pycurrents_ADCP_processing\project_data\CSIR_RDI_Sentin
el_FB_20150520_V3000.000"

metadata:
"\\"wsl.localhost\Ubuntu\home\ethan\adcp\pycurrents_ADCP_processing\project_data\CSIR_RDI_Sentin
el_FB_20150520_V3000_metadata.csv"
```

4. Change the destination directory

```
dest_dir = 'GB1_dir'
```

5. Run the script

In JL, go to File, New and open a terminal.

Activate the adcp37 environment in the JL terminal.

Navigate to ~/adcp/pycurrents_ADCP_processing

```
python pycurrents_ADCP_processing/create_nc_GB1.py
```

6.3 DATA PROCESSING IN PYCURRENTS:

6.3.1 L0 → L1: ADCP_processing_L0_L1.py

Purpose

Convert raw .pd0 (ping data format 0) ADCP data files (L0) into a self-describing NetCDF (L1) file. This is complete with georeferenced velocities, metadata, and basic QC.

Author

Hana Hourston

This script is adapted from Jody Klymak's at

<https://gist.github.com/jklymak/b39172bd0f7d008c81e32bf0a72e2f09> for L1 processing raw ADCP data.

Contributions from Di Wan and Eric Firing.

Inputs

- Raw .pd0 data file
- Deployment metadata in the form of a CSV. There is a template which denotes the required and optional information

Processing Steps

1. Metadata Processing

- Instrument time is converted to a *monotonic* (time always moves forward) time coordinate
- **create_meta_dict()**: Reads CSV metadata file containing deployment information
- **update_meta_dict()**: Extracts additional metadata from raw data files
- Processes instrument serial numbers, model identification, and geographic information
- Determines instrument orientation (*upward/downward facing*) and beam pattern (*convex/concave*)

2. Raw Data Reading

- Uses **pycurrents.adcp.rdiraw** library to read RDI ADCP files
- Extracts multidimensional variables:
 - *Fixed Leader*: System configuration data
 - *Velocity*: Current velocity measurements in beam coordinates
 - *Amplitude*: Backscatter intensity from each beam
 - *Correlation*: Signal correlation quality
 - *Percent Good*: Data quality metrics

3. Coordinate Transformation

- **coordsystem_2enu()**: Transforms velocity data from beam/XYZ coordinates to Earth coordinates (*East-North-Up*)
- Uses instrument heading, pitch, and roll data for transformation
- Applies beam angle and geometry corrections

4. Magnetic Declination Correction

- **correct_true_north()**: Rotates magnetic velocities to true geographic velocities

- Applies user-specified magnetic declination from metadata
- 5. Time Processing**
- **convert_time_var()**: Converts instrument time to standard UTC format
 - Handles time anomalies and out-of-bounds dates
 - Supports external time files for corrupted time data
- 6. Pressure Processing**
- **assign_pressure()**: Handles pressure data from various sources
 - For instruments without pressure sensors: calculates static pressure from depth
 - Uses *TEOS-10* equations for pressure-depth conversions
 - **check_depths()**: Validates instrument depth against pressure measurements
- 7. Data Quality Control**
- **flag_pressure()**: Flags negative pressure values
 - Sets *BODC* (British Oceanographic Data Centre) quality flags
- 8. Derived Variables**
- **compute_sea_surface_height()**: Calculates distance to sea surface
 - Computes sensor depth from mean pressure values
- 9. Dataset Segmentation**
- **split_ds_by_pressure()**: Handles mooring strikes by splitting datasets
 - **make_dataset_from_subset()**: Creates separate files for each time segment
 - Updates instrument depths based on pressure changes
- 10. NetCDF Creation**
- Organizes variables according to *CF conventions*
 - Adds comprehensive metadata and attributes
 - Applies proper encoding and fill values
 - Creates standardized variable names

6.3.2 Standardized Variable Names in L1 NetCDF Files

Velocity Variables

- LCEWAP01: Eastward current velocity (m/s) - *true north with magnetic declination correction applied*
- LCNSAP01: Northward current velocity (m/s) - *true north with magnetic declination correction applied*
- VEL_MAGNETIC_EAST: Eastward velocity (m/s) - *magnetic north, L0 processing only*
- VEL_MAGNETIC_NORTH: Northward velocity (m/s) - *magnetic north, L0 processing only*
- LRZAAP01: Upward current velocity (m/s) - *vertical velocity component*
- LERRAP01: Error velocity (m/s) - *beam 4, indicates data quality*

- LRZUVP01: Vertical beam velocity (m/s) - *Sentinel V instruments only*

Quality Control Variables

- LCEWAP01_QC: Quality control flags for eastward velocity
- LCNSAP01_QC: Quality control flags for northward velocity
- LRZAAP01_QC: Quality control flags for upward velocity
- LRZUVP01_QC: Quality control flags for vertical beam velocity
- PRESPR01_QC: Quality control flags for pressure

Acoustic Measurement Variables

- TNIHCE01-05: Amplitude intensity (acoustic backscatter) from beams 1-5 (*counts*)
- CMAGZZ01-05: Correlation magnitude from beams 1-5 (*counts*) - *data quality indicator*
- PCGDAP00, 02-05: Percent good data from each beam (%)
 - PCGDAP00: 4-beam solution
 - PCGDAP02: 3-beam solution
 - PCGDAP03: Transformations
 - PCGDAP04: Other
 - PCGDAP05: Vertical beam

Environmental/Instrument Variables

- PRESPR01: Sea water pressure at instrument (*decibars*)
- TEMPPR01: Water temperature at instrument ($^{\circ}\text{C}$)
- SVELCV01: Speed of sound in water (m/s)
- PTCHGP01: Instrument pitch angle (*degrees*)
- ROLLGP01: Instrument roll angle (*degrees*)
- HEADCM01: Instrument compass heading - magnetic (*degrees*)

Derived/Calculated Variables

- DISTTRAN: Distance from sea surface to each depth bin (m) - *sea surface height*
- PPSAADCP: Instrument depth calculated from pressure using *TEOS-10* (m)

Position and Metadata Variables

- latitude: Instrument latitude (*degrees_north*)
- longitude: Instrument longitude (*degrees_east*)
- filename: Original filename of processed data
- instrument_serial_number: Instrument serial number
- instrument_model: Instrument model and specifications
- instrument_depth: Depth of instrument below sea surface (m)
- water_depth: Total water depth at deployment site (m)

- geographic_area: Geographic area/region of deployment

6.3.3 L1 →L2: ADCP_processing_L2.py

Purpose

Apply physics-based and echo-intensity-based QC to mask non-ocean points (*air hits for up-lookers; sub-seafloor for down-lookers*) and generate QC diagnostics.

Author

Hana Hourston

Inputs

- L1 NetCDF file generated by **ADCP_processing_L0_L1.py**

Processing Steps

1. CTD Pressure Integration

- **add_pressure_ctd()**: Incorporates pressure data from co-located CTD instruments
- Handles different sampling intervals between ADCP and CTD
- Applies depth corrections based on instrument separation
- Creates *PREXMCAT* variable for CTD-derived pressure

2. Orientation-Specific Quality Control

For Upward-Facing Instruments:

- **flag_by_pres()**: Identifies bins above sea level (*negative pressure*)
- **flag_by_backsc()**: Detects surface contamination through backscatter analysis
- Uses beam-averaged backscatter increases to identify suspicious data

For Downward-Facing Instruments:

- **flag_below_seafloor()**: Flags measurements below seafloor depth
- Compares bin depths with water depth metadata

3. Advanced Flagging Algorithms

- **first_suspicious_bin_idx()**: Identifies where backscatter increases over consecutive bins
- Applies *BODC quality flags* (0=no QC, 1=good, 2=probably good, 3=probably bad, 4=bad)
- Uses 2D masking for efficient flagging across time-depth arrays

4. Data Visualization

- **plot_pres_compare()**: Compares static vs. CTD-derived pressure
- **plot_backscatter_qc()**: Shows quality control results with flagged regions
- Creates diagnostic plots showing *good, suspicious, and bad data*

5. Data Validation

- **bad_2_nan()**: Converts flagged data to NaN values (*optional*)
- **reset_vel_minmaxes()**: Updates data range attributes after QC

6.3.4 BODC Quality Flags

The processing uses the *SeaDataNet quality flagging scheme* from *BODC (British Oceanographic Data Centre)*:

Flag Value	Flag Name	Description
0	no_quality_control	No quality control has been applied to the data
1	good_value	Data has passed all quality control tests and is considered reliable
2	probably_good_value	Data is probably good but may have minor issues
3	probably_bad_value	Data is probably bad and should be used with caution (e.g., surface contamination)
4	bad_value	Data is bad/errorneous and should not be used (e.g., negative pressure, out of water)
5	changed_value	Data value has been changed by quality control processes
6	value_below_detection	Data value is below the detection limit of the instrument
7	value_in_excess	Data value exceeds the expected range or instrument capability
8	interpolated_value	Data value has been interpolated from surrounding measurements
9	missing_value	Data is missing or not available

Quality Flag Application

- **L1 Processing** automatically applies:
 - *Flag 0:* Default for all data (no QC initially applied)
 - *Flag 4:* For leading/trailing ensembles outside deployment period
- **L2 Processing** adds additional flagging:
 - *Flag 3:* For bins with surface contamination (backscatter increases)
 - *Flag 4:* For bins with negative pressure (above sea surface) or below seafloor

The quality control follows *CF-1.7 conventions* and uses the *SeaDataNet flagging scheme*, ensuring compatibility with international oceanographic data standards.